

# **CBET lolol**

(Hopefully soon to be Dr.) Philip W. X. Moloney

**IMPERIAL**

June 2024

Submitted in partial fulfilment of the requirements for the degree of  
Doctor of Philosophy of Imperial College London

Department of Physics  
Imperial College London  
Prince Consort Road  
London SW7 2AZ



# List of Acronyms

**Rad-MHD** Radiative-Magnetohydrodynamics

**Rad-Hydro** Radiative-Hydrodynamics

**HEDP** High Energy Density Physics

**LPIs** Laser-Plasma Instabilities

**CBET** Cross-Beam Energy Transfer

**ICF** Inertial Confinement Fusion

**PiC** Particle in Cell

**GO** Geometric Optics

**IB** Inverse-Bremsstrahlung

**SBS** Stimulated Brillouin Scattering

**PCGO** Paraxial Complex Geometric Optics

**IRT** Inverse Ray Tracing

**FRT** Forward Ray Tracing

**LLE** Laboratory for Laser Energetics

**LLNL** Lawrence Livermore National Laboratory

**CEA** Commissariat à l'Énergie Atomique et aux Energies Alternatives

**IAW** Ion Acoustic Wave

**OpenMP** Open Multi-Processing

**MPI** Message Parsing Interface

**inv-Brem** Inverse-Bremsstrahlung

**EI** Etalon Integral

**FL** Field Limiter

**CGT** Caustic Gain Truncation

**DPRs** Distributed polarization rotators



# 1 SOLAS, A 3-D Laser Ray-Trace and Cross-Beam Energy Transfer Model

This chapter will describe the SOLAS code, a 3-D Laser ray-tracing module implemented in the Radiative-Magnetohydrodynamics (Rad-MHD) code CHIMERA. The chapter begins with a discussion of why ray-tracing is frequently used to model ‘long-pulse’ lasers for High Energy Density Physics (HEDP) experiments and why the standard framework is inadequate to model Laser-Plasma Instabilities (LPIs). It will then go on to describe the ray-trajectory solver, electric-field reconstruction and Cross-Beam Energy Transfer (CBET) components of the model in detail. Discussion of the validity of the model components will be included. The numerical methods will also be presented alongside an extensive set validation problems to verify the implementation.

## 1.1 Ray-tracing for Hydrodynamic Simulations of Fusion Plasmas

Nanosecond length (‘long-pulse’) lasers are often used as an external energy source in the field of HEDP, for example in laboratory-astrophysics experiments [1–3], equation of state studies [4, 5] or Inertial Confinement Fusion (ICF) implosions [6–8]. Experimental design and analysis for these experiments must often be supported with fluid Rad-MHD simulations. The laser must therefore be described in these codes by a theoretical framework that is both valid to the problem and computationally tractable. The physical processes by which lasers interact with plasma is a result of microscopic couplings between the laser field and particles or plasma waves. The detailed microphysics of these interactions are often studied using Particle in Cell (PiC) codes [9] or wave-based solvers [10], typically for scales and durations of tens of micrometres and hundreds of picoseconds. Coupling these tools directly to multidimensional hydrodynamic simulations, which are often used for millimetre and nanosecond scales, would usually be computationally intractable.

The Geometric Optics (GO) assumptions are often applicable for HEDP laser-plasma interactions (validity discussed in detail for ICF plasmas in Sec. ??) and therefore ray-tracing offers a computationally tractable approach to modelling lasers in these experiments. By assuming static hydrodynamic profiles (which is normally valid for the propagation time of light through the computational domain) a laser beam can be discretized into a bundle of rays and the ray equations can then be integrated along their path to solve for the trajectory of the light, assuming that refraction dominates over diffraction. A discrete amount of power can also be given to each ray. If there is a suitable model for the power-absorption rate, this can also be integrated along the ray to provide an energy source for the plasma. In many

laser-driven HEDP experiments, frequency-doubled or -tripled lasers and long scale-length plasmas mean that Inverse-Bremsstrahlung (IB) is the dominant deposition process [11, 12]. There are well established models for IB that are suitable for implementation in ray-tracing codes, because they only require knowledge of the local plasma conditions, which are easily accessible via interpolation from the hydrodynamic grid to rays [13, 14]. The combination of the ray equations and IB deposition therefore is the basis for the vast majority of laser-modules coupled to hydrodynamic codes.

In laser-driven ICF experiments however, another class of interaction, LPIs are vitally important to the energetics of the implosion. For example CBET leads to a zeroth-order correction to the energy deposited in direct-drive experiments at the OMEGA laser facility, reducing coupled power late in the implosion to  $\sim 50\%$  [15]. LPIs cannot be included in the simple framework described above because they are non-linear<sup>1</sup> and reduced theoretical models of the interaction rely on knowledge of the electric field or intensity of the light [16]. Implementation in a tracing code therefore necessitates a method by which the separate light waves can ‘talk’ to each other. For example, the CBET code described in this chapter stores information for separate components of laser beams on a common grid which can then interact via the ‘pump-depletion iterations’, described in Sec. 1.5.5. Additionally, the knowledge of electric field or intensity is problematic because this is not an attribute which standard GO rays possess. Heuristically, rays have an associated power, so an area is required to obtain an intensity. The evolution of a portion of the beam front’s area is governed by a first order expansion of the Helmholtz equation, rather than the zeroth order expansion which is most commonly used in ray-tracing packages for hydrodynamic codes [17]. The first order expansion introduces an equation for the ray amplitude which can be solved in a variety of ways and used to obtain the electric field of the light. Sec. 1.4 describes the approach taken to solving for the amplitude of the rays in SOLAS, which is to track the area of a triangle<sup>2</sup> of rays around a standard GO ray.

For direct-drive ICF simulations, it is also desirable to have a 3D ray trace, where rays travel and refract in 3 dimensions. In some computational direct-drive studies, particularly in 1D hydrodynamic simulations, simplified laser models are employed in which rays travel radially toward the target [18]. This simplification is can lead to significant deviations from reality, as it neglects any refractive losses, which become increasingly significant late in the implosion as the target converges. Assuming that rays travel radially inward also leads to deposition occurring closer to the critical surface compared to a true 3D ray trace, leading to an overestimation of the drive. The growth of LPIs also depends on vector summations of light and plasma wavevectors, so a 3D ray trace is necessary when modelling these effects. Predictive direct-drive simulations therefore necessitate a fully 3D ray-trace, even when coupled to just 1D hydrodynamics.

---

<sup>1</sup>Non-linear in this context means that the interaction involves the interaction of multiple light and plasma waves.

<sup>2</sup>For a 2D ray trace, a pair of rays is used rather than a triangle.

## 1.2 Existing Cross-Beam Energy Transfer Models

There are a variety of existing computational tools used to model CBET for ICF conditions, which are used to study the interaction from first principles, reduced models to investigate the effect of CBET when coupled to hydrodynamics or validation tools to test the implementation of these reduced models. A non-exhaustive list will be presented here of existing codes, provided mainly as context for the work presented in this chapter.

### 1.2.1 Ray Based Models

The most common tool to study the coupling of CBET effects into hydrodynamics are reduced ray-based models which use the linear gain theory of Stimulated Brillouin Scattering (SBS), outlined in section???. There are a variety of different codes used to simulate this. The main difference between the models is the way that the electric field or intensity of the laser light is obtained.

**Inverse Ray Tracing (IRT)** This is an approach, implemented within the IFRIIT code, that creates a mapping between points on an initial beam front and arbitrary locations within the plasma [19, 20]. This is in contrast to Forward Ray Tracing (FRT), which is used in the other ray-based approaches listed below, where discrete points on the beam front are integrated forward to discrete points within the plasma. IRT is a very efficient approach for convex, approximately spherically symmetric plasma profiles, it can not deal well with beams that have multiple caustics<sup>3</sup>, where the FRT approach is better suited. IFRIIT has been coupled to the 3-D Radiative-Hydrodynamics (Rad-Hydro) code, ASTER from Laboratory for Laser Energetics (LLE), and prior to the development of SOLAS, ASTER-IFRIIT was the only code combination capable of conducting 3-D direct-drive simulations with in-line CBET [15].

**Ray Statistics Approach** The LASNEX [21], TROLL [22] and DRACO codes [23], developed at Lawrence Livermore National Laboratory (LLNL), Commissariat à l’Énergie Atomique et aux Energies Alternatives (CEA) and LLE respectively, implement field-reconstruction methods which depend heavily on having many rays per computational cell. LASNEX and TROLL, used mainly for indirect-drive hohlraum simulations, obtains the intensity of light by first propagating rays through the mesh and obtaining the deposited power in each grid cell. The intensity is then obtained from the power in each cell using electromagnetic energy conservation. Obtaining the intensity from deposition means that the field cannot be reconstructed in vacuum regions where no deposition occurs.

DRACO uses a similar approach, but the intensity is estimated by multiplying the ray power by the path length in a cell divided by the cell volume, which gives a dimensional estimate for the intensity. Both of these approaches require many rays-per cell to accurately obtain the intensity,  $\mathcal{O}(100)$  [24]. For direct-drive simulations this is extremely computationally expensive, because backscatter CBET dominates over sidescatter, therefore the reflected field

---

<sup>3</sup>Caustics are defined and discussed in detail in Sec. 1.4.1.

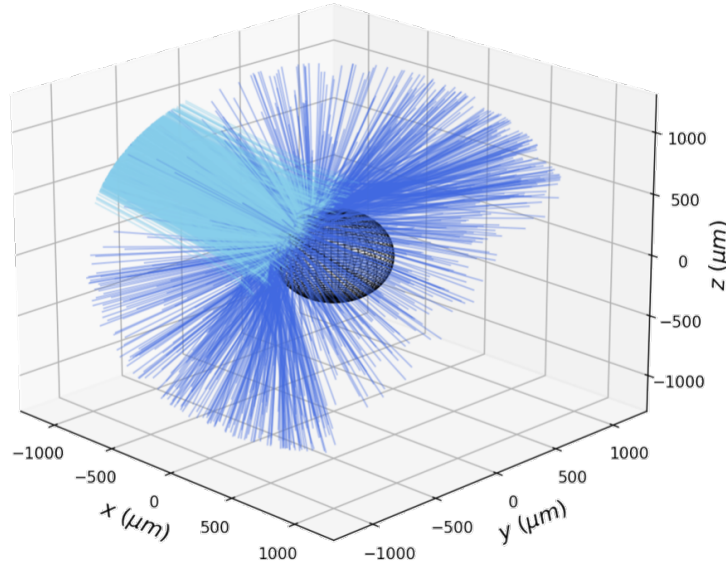


Figure 1.1: 3D ray trajectories through a spherically symmetric, OMEGA direct-drive scale density profile. The incident rays are plotted in cyan and the reflected rays, which spread out over a very large solid angle, are plotted in dark blue. The critical density is represented by the black mesh.

of each beam must be resolved, and each beam spreads out over a large solid angle after reflecting off a convex density profile, as is demonstrated in Fig. 1.1. This means that orders of magnitude more rays are required than for approaches which can accurately obtain the field from a single ray per cell.

Another drawback of both of these approaches is that caustics of beams (regions where the amplitude of rays diverge) are not identifiable, and therefore fields cannot be capped to physically accurate, diffraction-limited values. If a significant amount of CBET occurs at caustics, such as in direct-drive ICF, then erroneous global multipliers to CBET gains must be applied which are effectively free parameters that must be tuned to obtain a pre-known reduction in absorbed energy. This means that it is difficult to trust this approach for predictive direct-drive simulations.

**Paraxial Complex Geometric Optics (PCGO)** In this approach, each ray has an associated Gaussian intensity profile, the width of which is integrated along the ray trajectory [17, 25]. A single ray can be used per cell as each ray can have an intensity which is interpolated to the mesh, but the reconstructed field at caustics is not accurate and the width evolution is only valid for a short propagation distance. This approach was coupled to the CHIC 2 dimensional hydrodynamics code, but is difficult to extend to 3D as the implementation relied on interacting only rays whose centroids crossed, which does not generically occur in 3D for non-coplanar rays [26].

**Neighbouring Rays** The BEAMCROSSER code obtains an area for each ray by co-tracing a triangle of neighbouring rays around it that can be converted into a ray amplitude and there-

fore electric field from electromagnetic energy conservation [27]. Integrating the amplitude along the ray trajectory means that the caustics can be identified and therefore fields in those regions capped to diffraction limited values [28]. Each ray also has an individual field value, and it is therefore less dependent on ray-per-cell statistics than geometric models, such as that used in the DRACO code described above [29]. Sec. 1.4 describes the implementation of this approach into the CHIMERA 3D Rad-MHD code, which had not previously been used coupled to hydrodynamics in multidimensional simulations.

### **1.2.2 Wave Solvers**

Solving Maxwell's equations with coupling to a plasma background is a useful tool for the study of LPIs. The main code used in the ICF community that uses this approach is LPSE, which propagates light waves through a prescribed, spatially varying density, temperature and velocity profile in 1D→3D [10, 30]. It then solves the nonlinear coupling of electromagnetic waves by allowing first order plasma perturbations (obtained from the ponderomotive beat pattern between light), which then feed back into the wave propagation. The perturbative approach means that LPSE is limited to linear problems and the temporal and spatial resolution required to resolve the beat frequency mean that coupling to multidimensional Rad-Hydro simulations is not feasible. However, it is an extremely useful tool to validate implementation of CBET models, especially in situations like scattering at laser caustics, such as the test case presented in Sec. 1.5.7.2. It can also be used for many other important studies, such as the mitigation of LPIs via laser bandwidth and the effect of beam smoothing techniques on the growth rate of LPIs [31].

### **1.2.3 PiC Codes**

Both Ray based codes and LPSE are ill-suited to the study of LPIs in the non-linear regime, where the laser intensity becomes sufficiently large that the ponderomotive imprint on the plasma can no longer be treated perturbatively. Understanding this growth and saturation of LPIs in this regime is particularly important for ICF schemes with high peak intensities, such as during the ignitor spike in shock ignition pulses [32]. Often kinetic effects such as ion-trapping become important in non-linear saturation, where ions are trapped and then accelerated in the CBET induced Ion Acoustic Wave (IAW), leading to changes in the IAW phase velocity and therefore a loss of resonance [9]. PiC codes are therefore well suited to model this kinetic saturation, albeit over short timescales and in simulations that are not truly representative of direct-drive conditions, due to computational expense [33]. Kinetic modelling of CBET has demonstrated that the growth of LPIs can be a much more complex, time-dependent problem than is assumed by the linear-models used in ray-based codes, leading to larger net energy transfers [34].

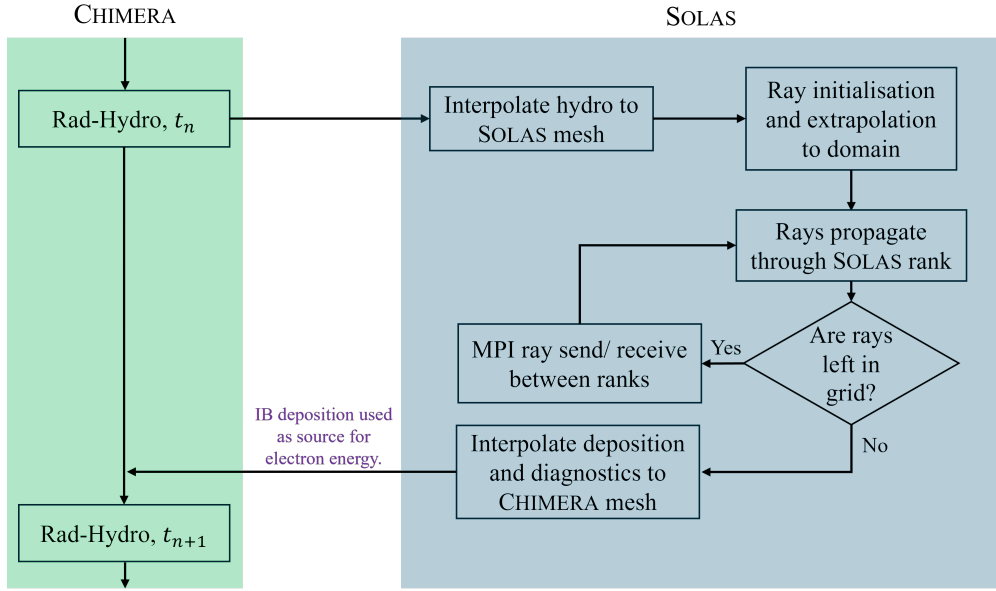


Figure 1.2: A flowchart illustrating the basic interfacing between CHIMERA and SOLAS. The interpolation steps refer simultaneously to the re-domain balancing and cell combination procedures described in Sec. 1.3.2.

## 1.3 SOLAS 3-D Laser Ray Trace

This section will describe how the ray equations, derived from the Helmholtz equation in Sec. ?? are solved in the SOLAS module for the CHIMERA Rad-MHD code. Details of the mesh used for spherical simulations and load balancing options shall be provided as well as validation problems.

### 1.3.1 Outline of SOLAS-CHIMERA Interfacing

A simple flowchart for the basic SOLAS operational loop and the interfacing with CHIMERA is shown in Fig. 1.2. At the start of a Rad-Hydro timestep,  $t_n$ , the hydrodynamic variables (stored on the Eulerian CHIMERA grid), which are necessary to compute ray trajectories and CBET gains are interpolated to the SOLAS mesh. Rays are then initialised on the beam port locations and extrapolated to the computational domain, before being traced through the grid. SOLAS uses a Message Parsing Interface (MPI) domain balanced approach to parallelization, the reasons for which will be discussed in more detail in Sec. 1.3.2, therefore rays are traced up to the internal borders of the domain subsection used for the MPI rank. Rays are then passed between ranks and moved through their new subdomain until they exit the entire simulation domain. As rays move through the domain, they contribute to total for Inverse-Bremsstrahlung (inv-Brem) deposition in each grid cell and other computational diagnostics. When all rays have exited the domain, the SOLAS quantities such as deposited energy which have been built up from the ray trace are then interpolated onto the CHIMERA grid, where the inv-Brem deposition is used as a source term for the electron energy in the subsequent Rad-Hydro step,  $t_{n+1}$ . The interpolation, initialization and propagation steps will be

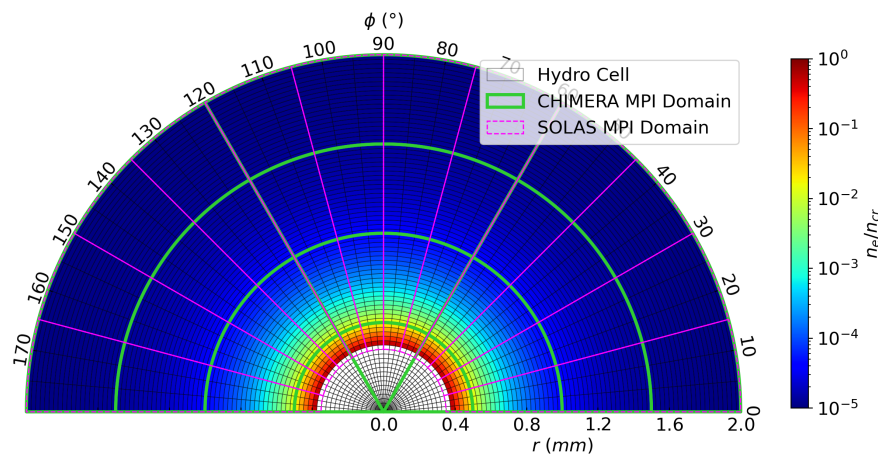


Figure 1.3: An illustrative diagram demonstrating the MPI re-domain balanced grid employed by SOLAS compared to the CHIMERA domain balanced grid for a cylindrical geometry.

outlined in sections 1.3.2, 1.3.3, 1.3.4 respectively.

### 1.3.2 SOLAS Mesh Structure

For direct-drive ICF simulations which model the laser using ray-tracing, especially those which include CBET, the choice of an appropriate computational mesh on which to conduct the laser ray-trace is crucial to obtaining an accurate and noise-free energy deposition. A well-chosen grid can also significantly reduce the run-time and memory requirements of the calculation. The mesh used for hydrodynamic simulations of these experiments is often not well suited for ray-tracing calculations. For example, hydrodynamic grid resolutions often have excessive resolution in the corona to resolve the gradients in the laser quantities, which greatly increases the expense of tracing rays through the mesh, without significantly enhancing the accuracy of the solution. This section will describe the approach taken in the SOLAS code to create a grid structure which is well suited to direct-drive simulations which we have found to accurately resolve laser energy deposition both with and without CBET in a memory-efficient manner.

#### 1.3.2.1 Re-Domain Balance for Radial Geometries

Rad-MHD codes often employ a domain balanced approach to parallelization<sup>4</sup>, where each computational rank solves a portion of the entire spatial domain each discrete timestep. Additional ‘ghost-cells’ are stored in the subdomains and used to calculate gradients on the boundaries between ranks, which are updated with inter-rank communications each timestep. The hydrodynamic grid for CHIMERA is Eulerian, with options for Cartesian, cylindrical or spherical-polar grids.

<sup>4</sup>This includes the CHIMERA code for which SOLAS has been developed.

The optimal domain balancing minimises communication between ranks, which leads to cubic<sup>5</sup> subdomains. If computing a laser raytrace through this domain however for a typical direct-drive calculation however, initially rays travel approximately radially and therefore regularly encounter processor boundaries where they must be transferred between ranks. A more optimal domain decomposition for the raytrace minimises radial splitting to avoid excessive passing of rays. When required for spherical and cylindrical simulations, SOLAS therefore takes the hydrodynamic variables on the CHIMERA grid and re-domain balances the grid for the raytrace, such that the splitting does not occur in the radial coordinate. An example of this re-domain balancing is shown in Fig. 1.3 for an illustrative cylindrical mesh. The CHIMERA domain decomposition divides the radial and azimuthal extent into 4 and 3 respectively, whereas SOLAS' division is purely in the azimuthal direction. For spherical and cylindrical direct-drive simulations where there is a defined, global minimum critical radius, SOLAS' mesh excludes the grid cells below this minimum radius beyond which the rays cannot reach in order to reduce the memory burden of the re-gridding.

An alternative approach to domain-decomposition parallelization of the module would be to use the Open Multi-Processing (OpenMP) package, where processors share memory across a computational node. In this approach, the entire laser grid would be stored once on the shared memory of the node and separate ranks would trace rays through the entire domain without the need for transfers. While this is certainly a preferable approach for a standard raytrace to the MPI procedure described above, including a model for CBET is more challenging with this approach. This is because CBET requires communication between beams and therefore large amounts of information must be stored on the grid, which can lead to large memory overheads. Therefore, using multiple computing nodes is often a necessity for 3D CBET calculations and OpenMP-MPI hybrid approaches are required which was deemed too significant an undertaking for the scope of the work presented in this thesis.

When a 3-D ray trace is coupled to a lower dimensional hydrodynamics simulation, for example, a 1-D spherical direct-drive simulation, then a sparse 3-D mesh at a user-specified resolution is created for the ray trace. This 3-D mesh allows the re-domain balancing routine to be employed to load balance the simulation. For CBET simulations, it also allows the field, which is required to compute the power change of rays due to CBET, to be stored as a function of angle when discretised on this sparse 3-D mesh. Storing the field discretised in angle enables the interaction between beams around the sphere to be correctly computed. After the ray trace, if these extra dimensions have been added to the ray trace grid, then the deposited power is integrated over the additional grid directions to obtain the source term on the hydrodynamic grid.

### 1.3.2.2 Semi-Structured Eulerian Grid with Combined Cells

Ideal ICF experiments are spherically symmetric and departures from this symmetry are usually next-order corrections to a spherical implosion. Simulations of these experiments therefore typically employ a computational grid with spherical symmetry. CHIMERA typically

---

<sup>5</sup>Cubic in cell dimension, not necessarily in physical space for non-Cartesian geometries.

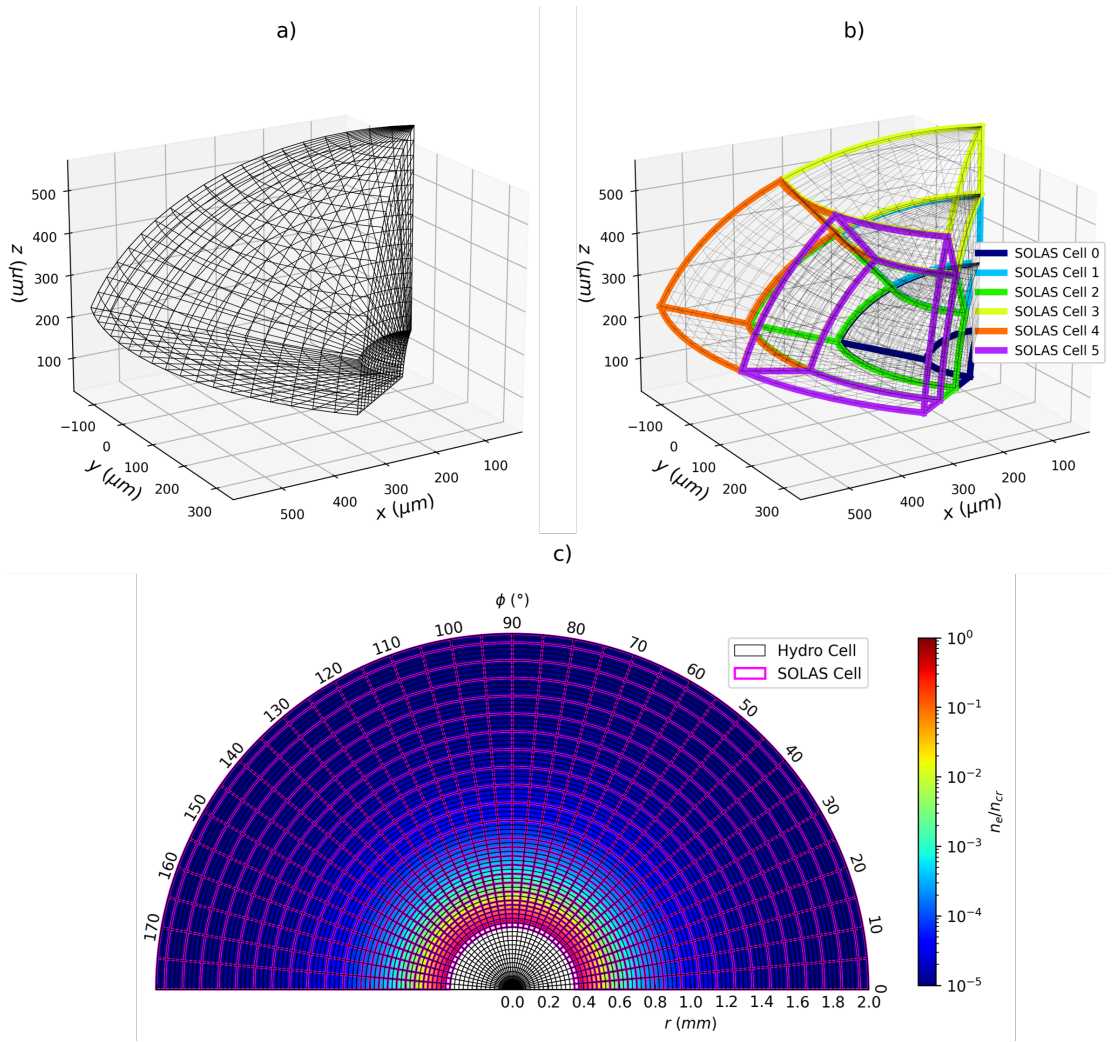


Figure 1.4: Illustrative diagrams demonstrating a) the spherical polar mesh used by CHIMERA for hydrodynamic calculations, b) the cell combination mechanism employed by SOLAS to obtain a roughly equal area grid for spherical simulations and c) the adaptive radial cell combination to reduce resolution in regions where CBET and refraction are unimportant.

simulates direct-drive implosions with a spherical-polar Eulerian mesh, shown in Fig. 1.4.a. This grid has the advantage of simplicity to take gradients across cells and develop new physics modules for the code, however it has the disadvantage that cell edge lengths go to zero as the radial coordinate,  $r \rightarrow 0$  and the polar coordinate,  $\theta \rightarrow 0, \pi$ . This limits the hydrodynamic timestep as stable explicit timesteps are inversely proportional to edge lengths, increasing the cost of 3D spherical simulations. The issue is circumvented at late times in the implosion by remapping onto a Cartesian grid, which does not have vanishing edge length and face areas [35].

Computing CBET however required at least a single ray from each interacting beam to pass through each computational grid cell where the interaction should be important. For spherical-polar meshes the vanishing cell volume therefore sets extreme minimum ray number limits for the calculation to fully resolve all the fields, especially for direct-drive simula-

tions due to the requirement to resolve the reflected fields which spread out over  $4\pi$  steradians, as is shown in Fig. 1.1. Hydrodynamic resolutions are often also excessive for ray trace calculations to resolve the necessary refraction and energy exchange of the light. Rays must stop at each cell boundary in order to deposit the correct amount of energy into each grid cell and therefore the expense of the ray trace is directly proportional to the number of grid cells that the rays see.

To circumvent this issue cells can be combined around the spherical grid angles in order to make a semi-structured Eulerian grid, as is shown in Fig. 1.4.b. Hydrodynamic grid cells are merged together on the SOLAS mesh in each grid direction until a pre-specified resolution, set by the problem is reached. In Fig. 1.4.b, many cells are combined in each direction to clearly display the effect. Typically, for spherical simulations however, the cells are not combined in the polar direction,  $\theta$  and  $n_\phi$  cells are combined in the azimuthal direction until the azimuthal and polar resolutions match, explicitly  $n_\phi r \Delta\phi \sin\theta \approx r \Delta\theta$  at a given radius,  $r$ .

Fig. 1.4.c demonstrates the capability of the meshing algorithm to adaptively combine cells in the radial direction based upon density gradients. This allows large cells to exist in the coronal plasma where the light refracts minimally and deposits little energy, while the sharp turning point regions close to the critical surface can be well resolved. To find the number of radial cells to combine at a given radius, the cell combination algorithm varies on the number of cells to combine  $n_r$  and calculates the maximum gradient length scale from all combined hydrodynamic cells,  $L_{n_e} = n_{crit}/|\nabla n_e|_{max}$ . The algorithm then finds the optimal number of cells to merge together such that the new cell resolution  $n_r \Delta r \approx C_L L_{n_e}$ , where  $C_L$  is a user parameter<sup>6</sup> which can be reduced to limit cell combining. A maximum cell size is also set to prevent excessively large cells in regions with minimal density gradients.

Note that many options for equal area computational grids exist which, unlike the semi-structured grid described here, are completely uncorrelated from the hydrodynamic mesh [36, 37]. These have the advantage that the grid can be completely chosen based solely upon the laser ray trace. However, the mesh described in this section has the advantage that interpolation to the hydrodynamic mesh is extremely straightforward as the SOLAS grid cells completely overlap the CHIMERA cells. This also removes minimises artefacts from interpolation between the grids, which have the potential to introduce spurious high order modes to the deposition source term.

### 1.3.3 Ray Initialisation

To obtain a noise-free energy deposition source term from a ray trace, both the grid and choice of initial rays number and location is crucial. The problems are closely related as a higher resolution grid will require a larger density of rays to get an equivalent ray-per-cell statistics. It is therefore wise to choose the number of rays used in a simulation to be some function of the grid used for the ray-trace. Several methods for ray initialization which have been implemented shall be briefly outlined here, along with a summary of their strengths and weaknesses.

---

<sup>6</sup>Default value set to  $C_L = 0.05$ .

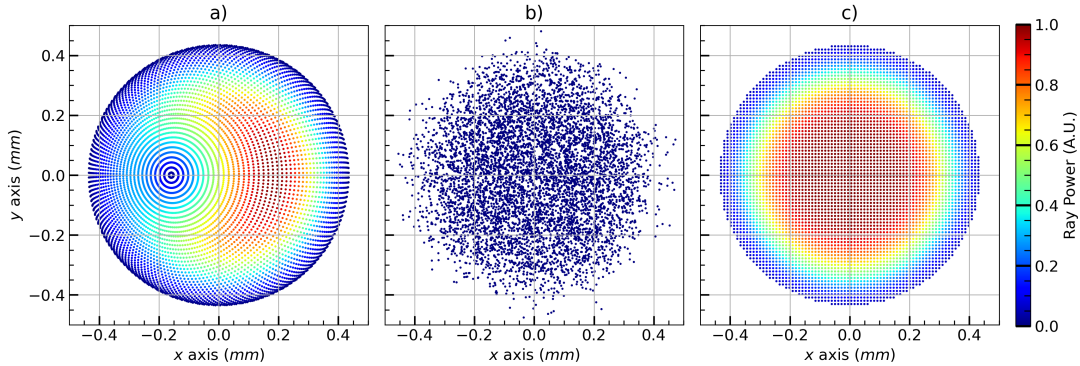


Figure 1.5: Example initial locations for  $\sim 4000$  rays for an OMEGA beam port with super-Gaussian intensity profile, with a shape defined by  $n_s = 5.2$  and  $\sigma = 352 \mu\text{m}$ . The inverse-projection ray locations are shown in sub-figure a) which demonstrate a higher ray density for rays pointed to the pole at  $x \sim -0.15\text{mm}$ . b) shows the randomly sampled rays where all rays are initialised with the same power, and c) shows uniformly sampled rays.

All beams profiles described in this thesis have circularly symmetric super-Gaussian intensity profiles described by the equation,

$$I(r) = I_0 \exp\left(-\left|\frac{r}{\sigma}\right|^{n_s}\right), \quad (1.1)$$

where  $r$  is the distance from the centre of the beam port, perpendicular to the beam normal,  $I_0$  is the peak intensity,  $\sigma$  is the beam width<sup>7</sup> and  $n_s$  is the super-Gaussian exponent.

**Uniform Sampling** In this method of ray initialisation, demonstrated in Fig. 1.5.c, each beam is assigned a number of rays and a maximum ray initialisation width<sup>8</sup>, beyond which rays are not initialised. Rays are then placed in a uniform, square grid on this plane with a power proportional to the intensity value from Eq. 1.1 and removed if their intensity is below  $I_0 e^{-3}$ , which gives the ray convex hull in 1.5.c the circular shape. For all three procedures described in this subsection, the total summed power of the rays is normalised to the incident beam power after the initialisation of all rays is complete. Typically, for direct-drive, the total number of rays used for spherical simulations is chosen to be,

$$N_{\text{ray}} = C_N \max(N_r N_\varphi, N_r N_\theta, N_\theta N_\varphi), \quad (1.2)$$

where  $N_{i=r,\varphi,\theta}$  is the number of SOLAS grid cells in that grid direction and  $C_N$  is a user-parameter multiplier which to give better ray statistics for CBET simulations when required.  $C_N \sim 2$  is found to give converged deposition when including CBET and so this value is used by default.

When there is sufficiently low ray-per-cell statistics, beat phenomena can occur between the ray spacing and the grid resolution. In this event, especially when using a nearest neighbour interpolation for ray power deposition onto the grid, significant spurious modes can be

<sup>7</sup>The radius at which  $I = I_0 e^{-1}$ .

<sup>8</sup>The maximum initialisation width is usually set to be the radius at which  $I = I_0 e^{-3}$ .

introduced to the power deposition. To resolve this, ray locations can be ‘dithered’ so that they take a random position within the polygon<sup>9</sup>, defined by neighbouring ray locations. This option is always used for simulations using uniform sampling in this thesis.

**Random Sampling** Rays can also be randomly sampled according to the intensity profile. Example ray locations from this method are shown in Fig. 1.5.b. Note that the intensity profile purely emerges from the ray locations in this method as all rays have equal power. For no CBET simulations this is a useful method as it minimises coherent build-up of noise from ray-spacing, grid-resolution beating. However, the wings of the intensity profile have very poor ray statistics so for direct-drive CBET calculations, resolving the reflected field and therefore the dominant backscatter CBET is excessively expensive.

**Inverse-Projection** Inverse-projection, is a final method that has been implemented for ray initialisation in SOLAS. The algorithm is described in detail in Appendix A of Ref. [23], but is not used for simulations in this thesis and therefore shall only be cursorily outlined. Briefly, the method works by finding several surfaces, defined by fractions of the critical density and then creating aim points in each cell on the surface. These aim points and their associated area on the surface are back-projected onto each beam port and rays are created if the aim point is not obscured by the surface on which it was created. The power of the ray is then the back-projected area multiplied by the intensity at the beam port location. For a spherical polar grid, this gives a ray distribution which varies in ray density according to which region on the beam port maps to regions on the grid with higher or lower cell-face areas. The rays in the higher ray density at the beam port region which maps to the polar region of the grid, at  $x \sim -0.16\text{ mm}$  on Fig. 1.5.a have a correspondingly lower power compared to rays at equal radii to give the same intensity.

While inverse-projection does guarantee good ray statistics at given surfaces for the in-bound component of the field, the algorithm does not extend to beyond ray caustics, or the reflected field component. Therefore, ray statistics are not guaranteed to be good for the reflected field, so the advantages of this method are not evident for direct-drive CBET simulations when backscatter must be resolved. However, for no CBET, direct-drive simulations, this is a useful option for ray initialisation.

For all simulations in this thesis, the uniform sampling method with ray dithering is used. This method is found to give the best ray-per cell statistics across the semi-structured Eulerian grid described in Sec. 1.3.2 while minimising the overall number of rays used required to resolve CBET.

After rays are initialised on each of the beam ports, rays are extrapolated to the edge of the computational domain. Beam focussing is typically neglected, so all rays are assigned velocities parallel to the beam normal. This approximation is widely used for codes that simulate OMEGA-scale direct-drive implosions, where the lasers are approximately collimated on the implosion scale [15, 23]. It is assumed that outside of the simulation domain is vacuum and

---

<sup>9</sup>This polygon is a square for uniform sampling, but not for inverse-projection

rays are therefore extrapolated to the edge of the computational domain in straight lines, using a simple root finding to find the intersection of the rays with either a spherical, cylindrical or rectangular domain depending on the simulation geometry.

### 1.3.4 Equations of Rays and Adaptive Integration

In SOLAS, each ray is defined by a position ( $\mathbf{x}$ ), wavevector ( $\mathbf{k}$ ), phase ( $\varphi$ ), angular frequency ( $\omega$ ) and power ( $P$ ). The partial differential equations that are integrated along the trajectory of each ray for these quantities are,

$$\begin{aligned}\frac{d\mathbf{x}}{d\tau} &= \mathbf{k}, \\ \frac{d\mathbf{k}}{d\tau} &= \frac{1}{2}\nabla\varepsilon(\mathbf{x}), \\ \frac{d\varphi}{d\tau} &= \varepsilon(\mathbf{x}), \\ \frac{d\omega}{d\tau} &= \frac{\omega}{2c}\frac{\partial(n_e/n_{cr})}{\partial t}, \\ \frac{dP}{d\tau} &= -\kappa_{IB},\end{aligned}\tag{1.3}$$

where  $\varepsilon = 1 - n_e/n_{cr}$  is the dielectric permittivity of the plasma,  $n_e$  &  $n_{cr}$  are the electron & critical densities,  $c$  is the speed of light,  $t$  is time,  $\kappa_{IB}$  is the inv-Brem absorption kernel, given explicitly in Eq. ?? and  $\tau$  is the ray path length. Note that the phase here is defined such that it has the same dimension as path length and therefore has spatial units. The wavevector is normalised such that  $|\mathbf{k}| = \sqrt{\varepsilon}$ . The optical path length is related to the arc length,  $ds$  by the variable change  $ds = d\tau\sqrt{\varepsilon}$ . In some formulations of the ray-tracing equations, the differential equations are written in terms of the arc length [23, 38], which is equivalent, but more complicated and without benefit. Note that the time,  $t$  is not related to the ray path length  $\tau$ , because an operator split approach is taken to the ray trace, such that the hydrodynamic variables are frozen and the ray trace finds the time independent trajectory of the light through these profiles. The path length  $\tau$  is therefore best seen as a parameterisation of the ray curve.

The frequency shift arises due to light propagating through a time varying refractive index. This causes successive wavefronts to bunch up (blue-shift) or rarify (red-shift), which occurs for a temporally increasing or decreasing  $n_e$  respectively [39]. This effect is only significant for the work presented in this thesis when calculating CBET. For direct-drive calculations at the OMEGA laser facility scale, this results in wavelength shifts of  $\Delta\lambda/\lambda_0 \sim \mathcal{O}(0.1\%)$ , which is typically negible for computing ray trajectories. However, the induced wavelength shift is relatively significant when calculating the CBET resonance and in direct drive can alter the spatial location where scattering is significant [15]. Neglecting time-dependent ionisation effects, which is a good assumption during peak-power for the approximately steady-state direct-drive corona where CBET occurs, the time derivative of  $n_e$  can be obtained by

assuming that  $n_e$  is advected with the bulk fluid,

$$\frac{\partial(n_e/n_{\text{cr}})}{\partial t} = - \frac{\iiint_V \nabla \cdot [(n_e/n_{\text{cr}})\mathbf{u}] dV}{\iiint_V dV}, \quad (1.4)$$

where  $\mathbf{u}$  is the fluid velocity and the integral is over a computational cell volume. Using the Divergence Theorem, this can be rewritten,

$$\frac{\partial(n_e/n_{\text{cr}})}{\partial t} = - \frac{\oint_S (n_e/n_{\text{cr}})\hat{\mathbf{n}} \cdot \mathbf{u} dS}{\iiint_V dV}, \quad (1.5)$$

where the integral on the numerator is now over the cell bounding area, with normal  $\hat{\mathbf{n}}$  [23].

**Adaptive RK45 Solver** The default ray evolution algorithm in SOLAS is to solve Eq. 1.3 using an adaptive RK45 algorithm with stepsize control [40]. Ray steps are either limited by the error from this algorithm, or by distance to the next impact with a cell face. Evaluations of the right-hand side of these equations employ trilinear interpolation for  $n_e$ ,  $\nabla n_e$  and  $T_e$  to obtain varying values for these quantities at different locations throughout the cell. All other quantities are either defined at the ray location, or use nearest neighbour interpolation. The `bspline-fortran` library has also been implemented to allow tricubic interpolation of  $n_e$ , which yields a quadratically varying  $\nabla n_e$  across the grid [41]. This is slow to evaluate many times per ray step as is required in an RK45 algorithm and therefore limits performance, but is used throughout this chapter as a higher order solution to validate accuracy of the default interpolation.

Linear interpolation of  $n_e$  and  $T_e$  is required for accurate computation of  $\kappa_{\text{IB}}$ , especially for ‘cold-start’ simulations where light impacts upon a solid target and the plasma profiles have steep gradients. Interpolation of  $\nabla n_e$  was found to be necessary to obtain low-noise ray amplitudes from neighbouring rays for CBET evaluation, which is described in more detail in 1.4. Linear interpolation of both  $n_e$  and  $\nabla n_e$  is technically inconsistent, because  $\nabla n_e$  should be the gradient of  $n_e$ , however the test cases presented in Sec. 1.3.4.1 found that this did not reduce accuracy compared to the Kaiser algorithm, which employs a self-consistent linear interpolation of  $n_e$  and constant  $\nabla n_e$  within a computational cell.

**Kaiser Algorithm** The Kaiser algorithm for ray integration has also been implemented [38]. In this algorithm, each cell has a single  $\nabla n_e$  and an  $n_e$  value defined at the cell centre, allowing for linear interpolation of  $n_e$  throughout the cell. In a constant  $\nabla n_e$  region, the trajectory of rays can be analytically shown to follow a parabola. The Kaiser algorithm thus evolves rays over parabolic segments between cells by finding the intersection of the parabola with cell faces, using a root finding algorithm. Assuming constant  $\nabla n_e$  cells leads to discontinuities in  $n_e$  at cell interfaces when the true gradient is not linear and thus Snell’s Law is used to refract rays upon cell exit. While this method is often slightly more efficient compared to the adaptive RK45, it was found that when attempting to reconstruct the ray amplitude from the area of neighbouring rays, as outlined in Sec. 1.4, excessive noise was introduced in the amplitude from the discontinuous refraction. Therefore, the adaptive algorithm was used

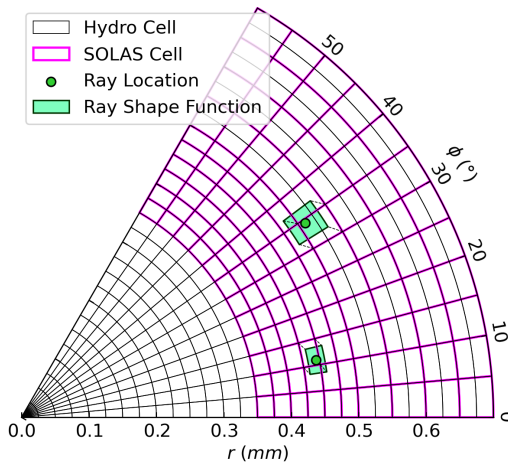


Figure 1.6: Demonstration of the shape function smearing weighting for ray power interpolation to the SOLAS mesh for a cylindrical mesh. The shape function has the same size and geometry as the SOLAS grid cell which the ray is located in. A top-hat shape function is used, so the fraction of the deposited power interpolated to a given cell is proportional to the volume overlap of the shape function with the cell.

for all work in this thesis, other than where explicitly outlined.

**Shape Functions for Ray Deposition** Nearest neighbour interpolation of power deposition, which is defined along the ray trajectory, onto the computational grid can result in significant levels of noise in the power deposition profile when ray statistics are not sufficiently high. This is similar to problems experienced in PiC codes when interpolating macro particles to the grid without the use of shape functions [42, 43]. A PiC-inspired shape function approach was taken therefore, where the power deposition from rays is smeared across neighbouring cells. A top hat shape function is used, with a shape function that has the size and shape of the cell that the ray is located within, as is shown in Fig. 1.6. The power deposited into each cell that has an overlap with the shape function bounds is therefore proportional to the volume overlap of the shape function with the cell. This approach is more explicitly outlined, particularly for the case of the non- logically rectilinear grids which are present for SOLAS, in Ref. [44]. This smearing is somewhat numerically diffusive and therefore can be optionally disabled. For the work presented in this thesis, the shape function smearing is employed for multidimensional direct-drive simulations, but otherwise disabled.

**Hydrodynamic Time Step Limiter** Laser heating of a plasma results in a temperature increase of the material, which also reduces the inv-Brem kernel. If the hydrodynamic timestep,  $\delta t$  is too large therefore, excessive heating will be deposited in initially cold cells, which should gradually in time have the magnitude of absorption reduced as they warm up. This can lead to spurious oscillations in temperature at fine grid resolutions. A limiter on the hydrodynamic time-step is therefore introduced to prevent large heating in any cell within

one timestep. We implement the limit detailed by Haines in Ref. [45], which estimates the increase in temperature of a cell from inv-Brem heating by assuming an ideal gas equation of state to derive,

$$\delta t = \min_{n \in \text{cells}} \left( \tilde{\delta} t, C_{\delta t} \frac{3}{2} \frac{n_{e,n} e T_{e,n} V_n}{P_n} \right), \quad (1.6)$$

where  $\tilde{\delta} t$  is the stable hydrodynamic timestep from other relevant physics,  $n_{e,n}$ ,  $T_{e,n}$ ,  $V_n$  &  $P_n$  are the electron density, electron temperature, volume and deposited power into cell  $n$ , and  $C_{\delta t}$  is a user defined stability parameter. By default, the parameter  $C_{\delta t}$  is set to 1, which is found to be adequate for most situations [45]. Note that Eq. 1.6 is only applied in cells where  $n_{e,n} > 1 \times 10^{-4} n_{\text{cr}}$ . Small amounts of deposition in these cells can lead to large temperature increases, which severely limits  $\delta t$ , despite the cells often being far from the region of interest, normally near critical, where the maximum deposition occurs. For simulations where a laser heats a solid, initially cold target, Eq. 1.6 mostly only affects the hydrodynamic timestep early in the simulation, after which the laser-heated plasma corona remains in a mostly steady-state unless there are very steep changes in incident power.

#### 1.3.4.1 Ray Solver Validation

Several validation problems have been conducted to verify that the ray solver has been implemented correctly. Here we present the quadratic trough and cylindrical helix test problems which compare the path of a single ray in a density profile to an analytic solution to verify that the ray solvers correctly obtain for the trajectory of light. The blast wave problem is also presented which is a test of inv-Brem absorption to an analytic solution in the absence of thermal conduction and hydrodynamic motion.

**Quadratic trough** The quadratic trough is a test of ray trajectory in a quadratic density trough, which admits an analytic solution of a periodically oscillating ray [38, 45]. The density profile used for the test is defined as,

$$n_e(y) = \frac{n_{\text{cr}}}{2} \left( 1 + \frac{y^2}{y_c^2} \right), \quad (1.7)$$

which for light with wavelength  $\lambda = 351$  nm, is initialised with  $n_{\text{cr}} = 9.049 \times 10^{21} \text{ cm}^{-3}$  and  $y_c = 5$  cm. The domain has bounds  $x \in [0, 25]$  cm and  $y \in [-5, 5]$  cm and a ray enters the domain at  $[x_0, y_0] = [0, 3]$  cm. Analytic integration of the first 2 lines from Eq. 1.3, yields the analytic trajectory as a function of ray path length,  $\tau$ ,

$$\begin{aligned} x(\tau) &= \tau \sqrt{1 - \frac{n_e(y_0)}{n_{\text{cr}}}}, \\ y(\tau) &= y_0 \cos \left( \frac{\tau}{\sqrt{2} y_c} \right). \end{aligned} \quad (1.8)$$

The analytic trajectory is compared to the solution from the adaptive solver (using both default interpolation and tricubic interpolation of  $n_e$ ) and the Kaiser algorithm in Fig. 1.7.

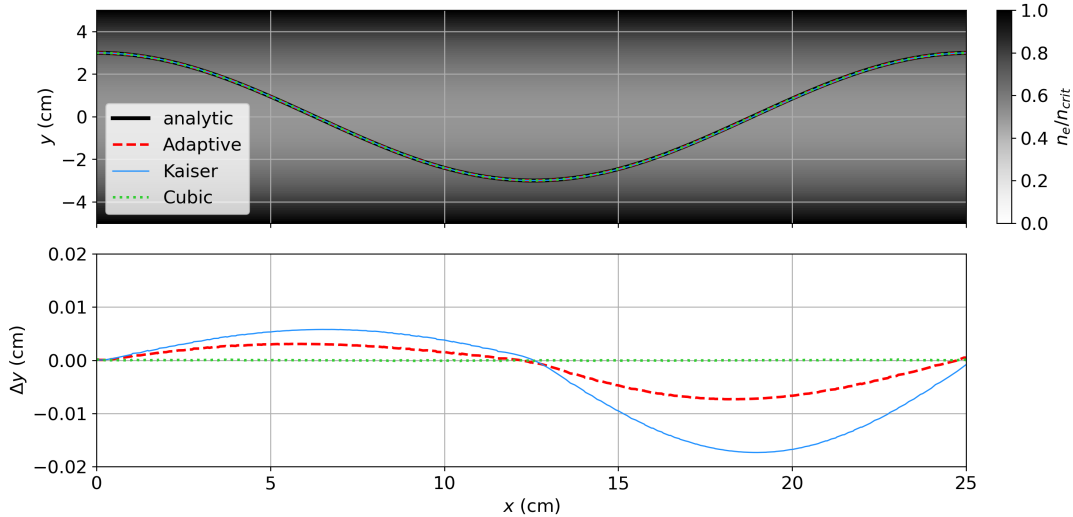


Figure 1.7: This figure demonstrates results of the quadratic trough ray trajectory test problem for the adaptive solver with 3 different cases. These are default settings (linear interpolation of both  $n_e$  and  $\nabla n_e$ ), the Kaiser algorithm (linear interpolation of  $n_e$  and uniform  $\nabla n_e$  in a cell) and the adaptive algorithm with tricubic interpolation of  $n_e$ ). The top plot shows ray trajectories and analytic trajectory and the bottom plot shows absolute errors for the 3 cases.

The associated error, defined as the difference in  $y$  at a given  $x$  is also plotted. Note that all results were obtained using a grid resolution of  $100 \times 100$  cells. The top panel demonstrates that all trajectories are identical to the analytic solution by eye. The corresponding errors show that the tricubic interpolation obtains effectively perfectly recreates the analytic solution and the Kaiser error is slightly more significant compared to the default adaptive error. The tricubic error is insignificant because the cubic interpolation perfectly recreates the true density profile, so the errors are purely numeric, not due to the resolution. Errors from the other algorithms would therefore decrease more quickly with increasing resolution as the density profile the ray sees becomes more similar to a quadratic trough. The error from the default adaptive interpolation (linear interpolation of both  $n_e$  and  $\nabla n_e$ ) is lower than that of Kaiser (linear  $n_e$  and uniform  $\nabla n_e$ ), indicating that the inconsistent interpolation is not a significant issue for resolving ray trajectories.

**Cylindrical-Helix** The quadratic trough test ensures that the ray evolution algorithm functions correctly in Cartesian geometry. An additional test was desired in non-Cartesian geometry, because CHIMERA also operates with cylindrical and spherical grids. The cylindrical-helix test was therefore devised, where a ray enters an axially symmetric density trough that keeps the ray at a constant, cylindrical radius,  $r$ , as is shown in Fig. 1.8.b. As is shown in Fig. 1.8.a, the  $z$  extent of the simulation is chosen such that the ray has performed one complete helical spiral when it exits the domain. By requiring that a ray undergo circular motion in the  $x - y$  plane and specifying the initial ray direction such that  $k_{z0} = \sqrt{k_{x0}^2 + k_{y0}^2}$ , it can be derived that a ray entering the domain at  $r_0$  will undergo one complete helical spiral over a

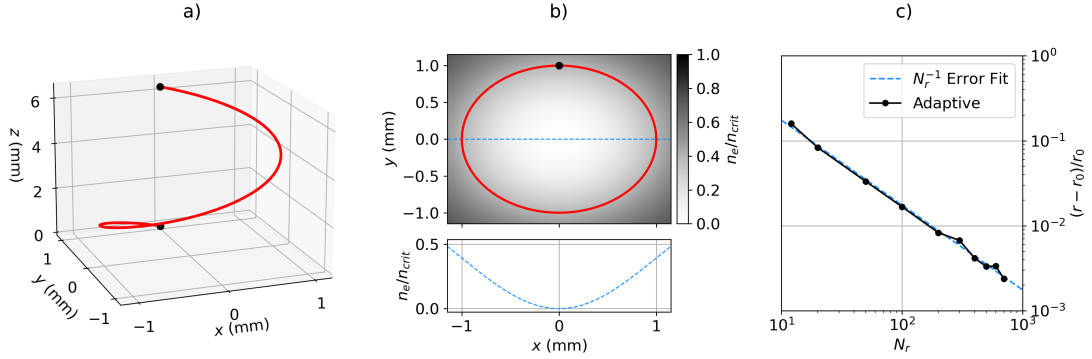


Figure 1.8: This figure illustrates the results from the cylindrical-helix test problem, obtained using the default adaptive RK45 algorithm. a) shows the trajectory of a ray with from a simulation with 100 radial cells in 3-D space. b) shows the trajectory of the ray projected on the  $x - y$  plane, along with the  $n_e$  profile. c) shows the error of the test, defined as the fractional difference in radius of the ray as it exits the domain from the initial radius, as a function of number of radial cells.

$z$  length  $\Delta z = 2\pi r_0$ , if the density profile has the shape,

$$n_e(r) = n_{\text{cr}} \left( 1 - \exp \left( \frac{-r^2}{2r_0^2} \right) \right). \quad (1.9)$$

For a ray entering the domain at  $[x_0 = 0, y_0 = 1, z_0 = 2\pi]$  mm, with initial wavevector  $[k_{x0} = \sqrt{\epsilon_0/2}, k_{y0} = 0, k_{z0} = -\sqrt{\epsilon_0/2}]^{10}$ , the ray position as a function of path length  $\tau$  is,

$$\begin{aligned} x(\tau) &= r_0 \sin \left( \sqrt{\frac{\epsilon_0}{2}} \tau \right), \\ y(\tau) &= r_0 \cos \left( \sqrt{\frac{\epsilon_0}{2}} \tau \right), \\ z(\tau) &= z_0 - \sqrt{\frac{\epsilon_0}{2}} \tau. \end{aligned} \quad (1.10)$$

The problem was run in cylindrical geometry for a variety of radial resolutions employing the default adaptive RK45 solver with linear interpolation of both  $n_e$  and  $\nabla n_e$ . The domain bounds for the problem were  $r \in [0, 1.5]$  mm,  $\varphi \in [0, 2\pi]$  &  $z \in [0, 2\pi]$  mm, with a single cell in both the  $\varphi$  &  $z$  directions. For all radial resolutions, the ray was observed by eye to exit the domain at the expected location, verifying that the ray trace is functional in non-Cartesian geometries. Plotting the fractional error in ray exit location as a function of number of radial cells,  $N_r$  in Fig. 1.8.c, demonstrates that the error in final position of the ray scales as  $N_r^{-1}$ . This is because larger  $N_r$  more closely recreates the density profile in Eq. 1.9. The error scaling is dictated by the error on the lowest order interpolation used in the algorithm, which is the linear interpolation of  $n_e$  for the default adaptive RK45 solver, which yields the  $N_r^{-1}$  scaling.

<sup>10</sup>  $\epsilon_0 \equiv \epsilon(r = r_0)$ .

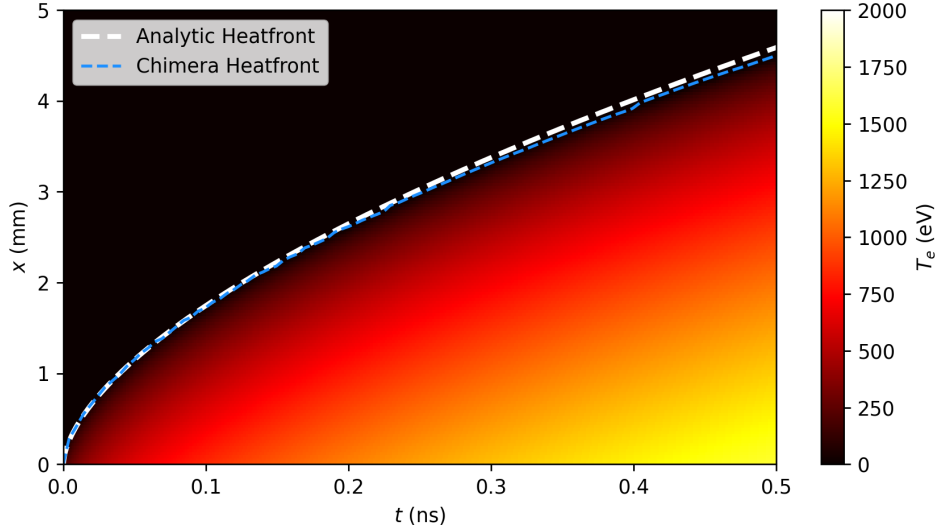


Figure 1.9: This figure shows the results of the blast wave inv-Brem absorption test problem. The colour-plot shows the temperature of the 1-D simulation as a function of time ( $x$ -axis) and space ( $y$ -axis). The heatfront obtained from CHIMERA, which is the maximum  $x$  location where  $T_e > T_{e0}$ , is in good agreement with the analytic solution.

**Blast wave** The blast wave problem is a validation test of the implementation of inv-Brem absorption [45, 46]. In this problem, a 527 nm, 2 ns laser is incident on a uniform density ( $\rho = 1 \text{ mg/cm}^{-3}$ ), cold gas ( $T_{e0} = 1 \text{ eV}$ ) with fixed ionisation at  $Z = 6$ , that has an ideal gas equation of state. The  $\ln \Lambda$  value used for the  $\kappa_{IB}$  coefficient is fixed at 7. The laser travels in the  $x$  direction and has an intensity of  $6.4 \times 10^{13} \text{ Wcm}^{-2}$ . Hydrodynamic motion and transport is disabled in the simulation. The laser is initially very strongly absorbed in the gas, so energy is not transported beyond the initial layer, perpendicular to the laser propagation direction. As the gas heats up,  $\kappa_{IB}$  decreases and therefore more energy is transported further into the domain by the laser, moving the heatfront forward. The heatfront  $x_{\text{analytic}}(t)$ , defined as the largest  $x$  coordinate at a time,  $t$  where  $T_e > T_{e0}$ , has an analytic solution under these assumptions, derived by Denavit and Phillion [46],

$$x_{\text{analytic}}(t) = \frac{2}{3\kappa_{IB}} \left( \frac{5}{3} \frac{\kappa_{IB} I}{n_e k_B} \right)^{3/5}, \quad (1.11)$$

which can be compared to the result from a ray-tracing simulation.

Fig. 1.9 shows the results for  $T_e(x, t)$  and the heatfront location from a CHIMERA-SOLAS simulation of the blast wave problem. The heatfront from the simulation compares well to the analytic heatfront, validating the implementation of the inv-Brem absorption kernel.

## 1.4 Ray Based Field Reconstruction and Ray Sheets

In order to compute CBET, or other LPIS in a ray-tracing calculation, additional information about the electric field or intensity of the light is required than can be obtained from the ray

directly from the routine outlined in Sec. 1.3. In this section the method used in SOLAS to obtain the electric field of the light along the path of each ray shall be outlined. This broadly follows the implementation from Ref. [29].

### 1.4.1 Ray-Amplitude & Field Estimate from Neighbour Rays

Recalling the formula for the ray-amplitude,  $A$ , Eq. ?? from Sec. ??,

$$A(\tau) = A(0) \left| \frac{D(0)}{D(\tau)} \right|^{1/2}, \quad D(\tau) = \begin{bmatrix} \frac{\partial x}{\partial \zeta_1} & \frac{\partial x}{\partial \zeta_2} & \frac{\partial x}{\partial \tau} \\ \frac{\partial y}{\partial \zeta_1} & \frac{\partial y}{\partial \zeta_2} & \frac{\partial y}{\partial \tau} \\ \frac{\partial z}{\partial \zeta_1} & \frac{\partial z}{\partial \zeta_2} & \frac{\partial z}{\partial \tau} \end{bmatrix}, \quad (1.12)$$

where  $[x, y, z]$  and  $[\zeta_1, \zeta_2, \tau]$  are the ray real-space and phase-space coordinates respectively and  $D$  is the Jacobian for the coordinate transform from phase-space to real-space. When refraction forces rays closer together,  $|D(\tau)|$  will decrease and equally, when refraction forces rays to separate,  $|D(\tau)|$  will increase. The amplitude can therefore be approximated by assuming proportionality between the determinant of the Jacobian and the area,  $S$  of an infinitesimally small bundle of rays surrounding the main ray,

$$A(\tau) = \varepsilon^{-1/4} \sqrt{\frac{S(\tau=0)}{S(\tau)}}, \quad (1.13)$$

where the  $\varepsilon^{-1/4}$  term accounts for swelling of the field due to the increased optical path through plasma with finite density [29]. Note that the amplitude is a purely geometric quantity, which holds no information about power changes of the light from absorption or LPIs. The electric field outside the caustic region, which shall be discussed in more detail in Sec. 1.4.2, can then be obtained with the formula,

$$\frac{|E(\tau)|}{|E(\tau=0)|} = \sqrt{\frac{P(\tau)}{P(\tau=0)}} A(\tau), \quad (1.14)$$

where  $P$  is the power of the ray and the initial (vacuum) electric field  $|E(\tau=0)| = \sqrt{2I_0/c\varepsilon_0}$ , where  $I_0$  is the intensity of the beam at the ray initialisation point on the beam port.

This method, which has been used successfully to model direct-drive CBET in the BEAM-CROSSER post-process code, is the approach taken to estimate the field in SOLAS. Explicitly, for every ray that initialised for a SOLAS calculation, an additional 3 ‘neighbour-rays’ are initialised in an equilateral triangle around it, perpendicular to the initial direction of propagation at a random angle. Note that when a 2-D ray-trace is used, only 2 neighbour-rays are required as the rays cannot change separation in the out of plane direction. It is important to distinguish the dimension of the ray-trace, which is the number of dimensions in which rays can move in a simulation, to the dimension of the hydrodynamics. For example, a 1-D spherical direct-drive Rad-Hydro simulation still requires a 3-D ray trace where rays can move in  $x, y \& z$  for full accuracy.

These neighbour-rays are then co-traced up to the phase of the ‘main-ray’ to evaluate the

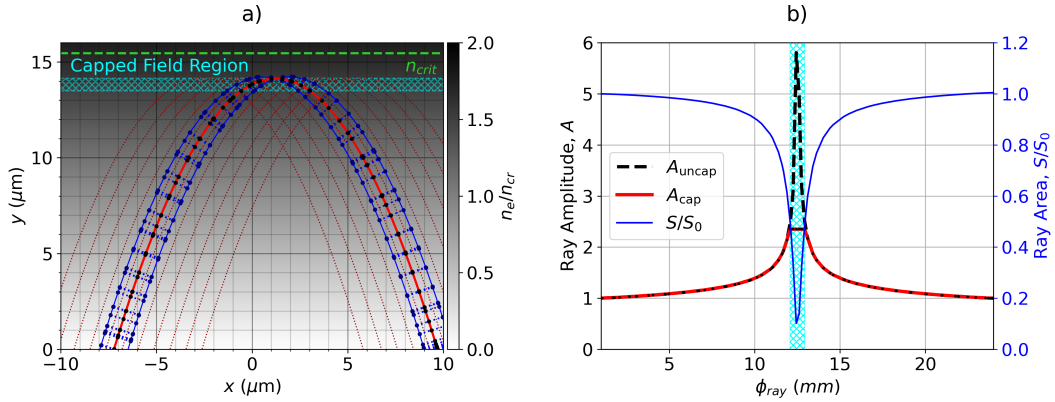


Figure 1.10: This illustrative figure demonstrates how the ray-amplitude is obtained from the area of neighbouring-rays for a beam propagating up a linear density gradient. Fig. a) explicitly shows the trajectory of a main-ray and its neighbour-rays in red and blue respectively, explicitly highlighting the beam's caustic region, where the amplitude of the light is capped. Fig. b) plots the area of the main-ray in blue, which goes through a minimum at the caustic location as a function of the phase of the ray. Also shown are the uncapped and capped amplitudes of the ray.

area of the main ray on its phase front. Practically, the separation distance of the bundle of neighbour-rays (i.e. the side-length of the triangle,  $\Delta l$ ) does not need to be infinitesimally small, but small enough that it accurately captures the local change of  $|D(\tau)|$ . In terms of the hydrodynamic profiles, this means that  $\Delta l \ll L_{n_e}$ , where  $L_{n_e}$  is the density length scale of the plasma. For OMEGA scale direct-drive simulations, an initial separation of  $\Delta l \lesssim 1 \mu\text{m}$  is found to give converged behaviour. If the separation is too small however, floating point arithmetic can lead to noise in the ray-amplitude estimation. For all simulations presented in this thesis,  $\Delta l = \lambda_0/10 \ll 1 \mu\text{m}$  was used.

As was mentioned in Sec. 1.3.4, it was found that the Kaiser algorithm for ray propagation, which uses a single  $\nabla n_e$  in each grid cell and discontinuously refracts rays at cell boundaries, led to large levels of noise in the ray-amplitude profiles. In order to obtain smooth profiles for  $A$ , linear interpolation of  $\nabla n_e$  was found to be necessary. The continuously varying  $\nabla n_e$ , which does not have discontinuities across cell interfaces, allows a smoothly varying area for each ray to be obtained.

Fig. 1.10.a demonstrates this amplitude reconstruction process in a purely illustrative example of a beam travelling up a linear density gradient at an angle, leading to a caustic at its turning point. The trajectory of several main-rays are plotted in dark-dashed red, and a single main-ray is highlighted in a brighter shade of red. The 2 neighbour-rays of this highlighted main-ray are plotted in blue. Note that in this figure, the default initial main-neighbour-ray separation of  $\Delta l = \lambda_0/10 = 0.035 \mu\text{m}$  was used, but the separation has been magnified on the plot to visualise the amplitude reconstruction from the area more clearly. The locations of the main- and neighbour-rays after a single step of each main-ray are plotted as black and dark-blue spots respectively. The 'area' of the neighbour-rays  $S$ , which in

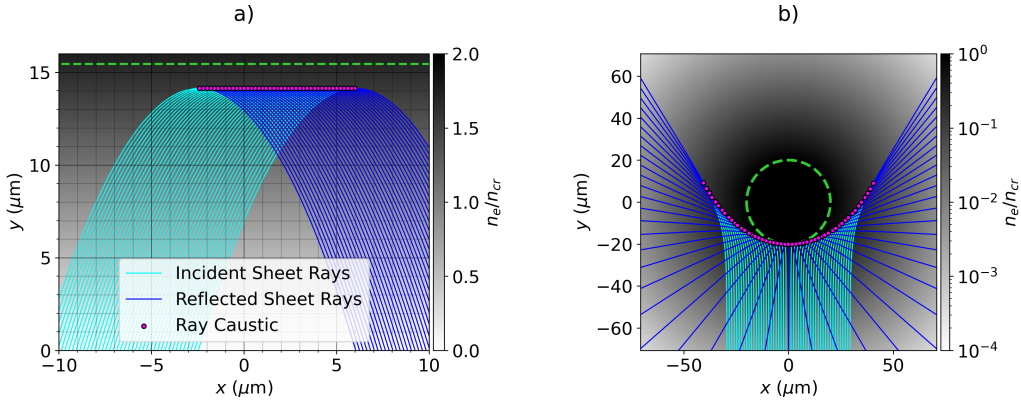


Figure 1.11: This illustrative figure illustrates the concept of caustics and ray sheets. In a), the trajectory of ray traversing up a linear density gradient are plotted. Separate colours are used for the incident and reflected sheets, which are separated by a caustic. In b), rays propagate up a density profile,  $n_e = n_{cr} \exp [-(r_{\mu m} - 20)/100]$ . Unlike in a), the ray caustics do not occur at their turning point, *i.e.* the minimum radius.

this 2-D raytrace example here is simply a distance, is plotted on 1.10.a as a dashed blue line between the neighbour-rays. The neighbour-rays are pushed until they have the same phase as the main-ray,  $\varphi_{ray}$ , at which point the area is evaluated.

#### 1.4.1.1 Caustics and Ray-Sheets

Caustics are an important concept in GO, and the reconstructed field in their vicinity must be handled correctly in order to accurately model CBET in ray based codes. Fig. 1.10.b plots the area of the main-ray as a function of main-ray phase in blue. At  $\varphi_{ray} \sim 12 \mu m$ ,  $S \rightarrow 0$ , *i.e.* neighbouring-rays cross over each other, which is known as the ray-caustic. In the absence of caustics, rays never cross over each other and therefore the mapping from ray phase-space (beam-port locations, where  $\tau = 0$ ) to real-space is single valued, or in other words each point in space will be reached by (at most) one ray from each beam. In the presence of caustics, this single valued mapping breaks down and a single real-space location is accessible by multiple ray launch locations. A single valued mapping is still possible if each beam is separated into distinct ‘sheets’ after caustics, where each sheet still has a single-valued projection from phase-space to real-space.

This is illustrated in Fig. 1.11.a, where rays from a single beam are plotted propagating up a linear density gradient with  $n_e = n_{cr} y_{\mu m} / 15.5$ . As the density gradient is purely in the  $y$  direction, each ray has translational symmetry in  $x$  and therefore each ray-caustic is located at the ray turning point,  $y \sim 14 \mu m$ . The portions of the ray trajectories that fall before and after the caustic are separated into the ‘incident’ and ‘reflected’ sheets respectively and plotted in separate shades of blue. Fig. 1.11.b also plots rays from a single beam, but now propagating through a cylindrically symmetric  $n_e$  profile. As can be seen from this figure, the caustic is

not the same as the ray turning-point<sup>11</sup>, but the location that the amplitude diverges.

This means that unless the amplitude is tracked along each ray trajectory, the location of the caustic cannot be identified and rays cannot be separated into distinct sheets, both of which have important ramifications for ray-based CBET models. Firstly, because the amplitude diverges, the field values can become very large and therefore must be capped to diffraction limited values, the method for which is discussed in more detail in Sec. 1.4.2. Additionally, if the beam cannot be separated into distinct sheets, then self-CBET, where the reflected component of a beam interacts with the incident component of the same beam, must be neglected. In SOLAS, the neighbour-ray method allows the amplitude to be tracked along each ray, enabling caustic location and sheet-separation. Currently, it is assumed that each sheet has 2 sheet components, *i.e.* an incident and reflected field, but it should be possible to extend this to multiple caustics to accurately model complex CBET interactions such as target-stalk simulations [47–49]. This is an advantage of the forward ray tracing approach to CBET modelling compared to inverse-ray-tracing, where only plasma profiles that result in a single caustic can be modelled [15].

The phase of the light is also evolved along each ray trajectory in equations 1.3, and therefore the coherent sum of all electric fields can be reconstructed which involves interference between sheets. The total electric field is,

$$E = \sum_{j \text{ sheets}} |E_j| \exp(i(k_0\varphi_j - \pi\alpha_j/2)), \quad (1.15)$$

where  $k_0$  is the vacuum wavevector of the light and  $\alpha_j$  accounts for the  $\pi/2$  phase shift that occurs when a ray changes sheet, *i.e.*  $\alpha_j = 0$  for the incident sheet and  $\alpha_j = 1$  for the reflected sheet [29].

The fields are discretised on the SOLAS mesh by nearest neighbour interpolation from the ray to the cell. When multiple rays from the same sheet pass through a cell, then the inverse-distance weighted average of the mid-point along the ray step to the cell centre is used to compute the field value for the cell. This leads to a field structure,  $|E_j|(\mathbf{x}, \mathbf{k}, \omega, \phi)$ , where  $j$  refers to each sheet,  $\mathbf{x}$  is the spatial location of the field which refers to the cell the field is stored in, and  $\mathbf{k}, \omega, \phi$  are the wavevector, frequency and phase of the ray. For many beam simulations, there is a very large associated memory cost to store this information on the mesh, which is discussed in more detail in Sec. 1.5.4. When computing the effect of CBET, it is also necessary to interpolate the fields stored at the cell centre to the ray trajectories. Nearest neighbour interpolation is also used for this step, so rays experience a constant value for  $|E_j|(\mathbf{x}, \mathbf{k}, \omega, \phi)$  throughout the cell. It would be technically be possible to use higher order interpolation for both stages, either from an unstructured mesh of the ray locations, or from the SOLAS mesh, which is close to logically rectilinear. The second of these options was tested but proved both to be the dominant computational cost for many beam CBET interactions and also challenging to robustly implement for non-Cartesian meshes, because the angular resolution for typical spherical direct-drive simulations was too coarse for the required accuracy.

---

<sup>11</sup>Defined here as the location of maximal  $n_e$  experienced along the ray trajectory.

### 1.4.2 Caustic Field Capping

In the vicinity of beam-caustics, the electric field magnitude of a beam is limited by diffraction which is neglected in GO, so ray based models which do not cap fields near caustics can experience divergent electric fields. For direct-drive simulations, significant amount of CBET occur near caustics and therefore sensibly capping the field value is crucial for accurate simulations [20]. This cannot be achieved without knowledge of the caustic location, which is a severe limitation to the predictive capability of CBET codes that do not track the amplitude. This section shall describe two methods that have been implemented to cap the field values in the vicinity of laser caustics, the Field Limiter (FL) and Etalon Integral (EI) approaches.

**Field Limiter** This is a straightforward hard cap on the maximum value of the electric field reconstructed during the ray trace. The electric field of light propagating up a linear density gradient has the analytic solution of an Airy function. The field limiter approach is to cap all electric fields to this value,

$$\frac{|E|}{|E(\tau = 0)|} = \sqrt{\frac{P(\tau)}{P(\tau = 0)}} \min \left[ A, \sqrt{\zeta} \left( \frac{n_t}{n_{cr}} \right)^{1/4}, \sqrt{\zeta} \sqrt{\frac{S(\tau = 0)}{S(\tau)}} \right],$$

$$\zeta = 0.9 (\omega L/c)^{1/3},$$

$$L = n_{cr}/|\nabla n_e|_t,$$
(1.16)

where  $n_t$  is the electron density at the caustic,  $|\nabla n_e|_t$  is the magnitude of the electron density gradient at the caustic location [28, 50, 51]. The first term in the minimum is the standard field reconstruction from the amplitude away from caustics. The second term is the maximum of the Airy function and the third term is an improvement to the second term for near-normally incident rays [29]. Fig. 1.10.b shows the capped amplitude obtained from the field limiter approach.

**Etalon Integral** The EI method is an improvement to the FL, which allows for deviations in the density profile away from linearity [19, 52, 53]. Several distinct types of caustic exist for different geometries of problem. For example in direct-drive, the light reflecting from the critical surface forms a ‘fold’-type caustic, whereas focussing light leads to a more complex ‘cusp’-type caustic [54]. If the form of the caustic is assumed, then an approximation of the total field in the vicinity of the caustic is formulated which allows for deviations from the ideal case. In the example of the direct-drive fold caustic, the field is assumed to be the sum of an Airy function and its derivative, which accounts for the deviations from linearity. An expression for the total field can be derived in terms of the ray-amplitude and phase before

$(A_1, \varphi_1)$  and after  $(A_2, \varphi_2)$  the caustic,

$$\begin{aligned} E_T &= \sqrt{\pi} [(-\xi)^{1/4}(A_1 + A_2)\text{Ai}(\xi) - i(-\xi)^{1/4}(A_1 - A_2)\text{Ai}'(\xi)] e^{i(k_0\chi - \pi/4)}, \\ \chi &= \frac{1}{2}(\varphi_1 + \varphi_2), \\ \xi &= -\left[k_0 \frac{3}{4}(\varphi_2 - \varphi_1)\right]^{2/3}, \end{aligned} \quad (1.17)$$

where  $\text{Ai}$  and  $\text{Ai}'$  are the Airy function and its derivative. In SOLAS,  $\text{Ai}$  and  $\text{Ai}'$  are computed numerically using the special-functions library [55]. This total field can then be divided between the incident and reflected sheet by inversion of Eq. 1.15 assuming that  $|E_1| = |E_2|$ ,

$$\frac{|E_j|}{|E_{j,0}|} = \frac{\sqrt{W_j} |E_T|}{\sqrt{2} [1 + \sin(\varphi_2 - \varphi_1)]^{1/2}}. \quad (1.18)$$

The assumption of equal fields is approximately valid for OMEGA scale direct-drive conditions, where the caustic region is small compared to the plasma scales and therefore ray powers are assumed to not vary significantly over this distance. The Etalon integral is applied in the ‘caustic-region’, which in Refs. [19, 56, 57], is stated to be equivalent to,

$$|\varphi_1 - \varphi_2| \leq \lambda_0/2, \quad (1.19)$$

where  $\lambda_0$  is the vacuum wavelength of the light.

Applying the EI method requires evaluation of Eq. 1.19 to determine if a ray is inside its caustic region, which relies on interpolation of the phase of the other sheet from the same beam onto the ray location. If using nearest neighbour interpolation, which is used in SOLAS for interpolation of all field quantities onto rays, this means a resolution of  $\Delta \ll \lambda_0$  must be used, which is a much higher resolution than is required for ray-tracing and CBET without the EI. Therefore, the EI method is only used in SOLAS simulations for very high resolution grid test problems, such as those Sec. 1.4.3. The alternative approach would be to implement linear interpolation from the field quantities all beams onto ray locations such as in Ref. [29]. This was not deemed a viable approach however, because the mesh resolution for spherical simulations was found to not be well-enough angularly resolved to interpolate the phase with sufficient accuracy to the rays. The standard procedure for CBET simulations in Solas is to use the FL approach which is found to give satisfactory results compared to the EI method.

### 1.4.3 Field Reconstruction Validation

In this section several test problems will be presented that compare electric fields obtained using SOLAS field solver in the absence of CBET, to those from the wave based solver LPSE in direct-drive relevant plasma profiles. The LPSE results are presented in Ref. [29], and are available from the repository [58]. In all the following test problems, the laser has a vacuum wavelength,  $\lambda_0 = 0.351 \mu\text{m}$  and a Super-Gaussian intensity profile,

$$I(r) = I_0 e^{-(r/\sigma)^{ns}}, \quad (1.20)$$

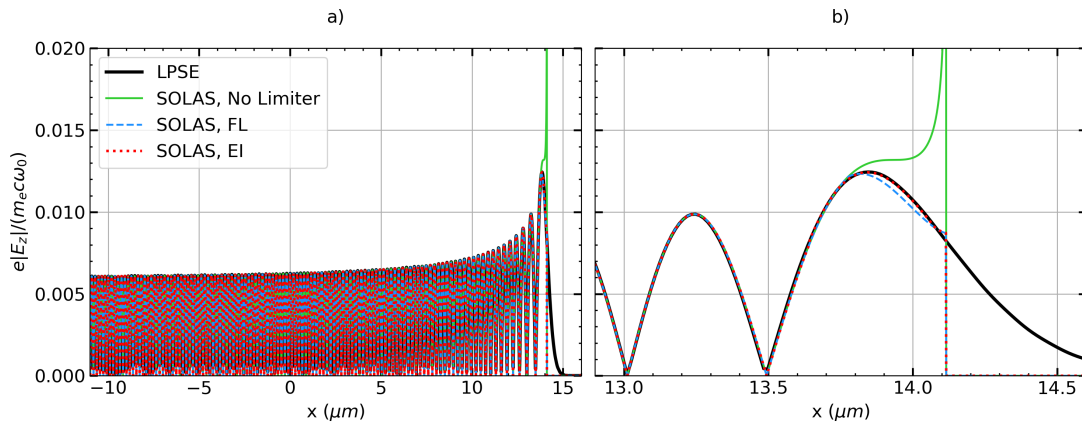


Figure 1.12: This figure shows the results of the 1-D field reconstruction test, comparing SOLAS fields with different caustic field capping methods to the LPSE results. Figure a) shows the oscillatory behaviour of the field solution which arises due to the interference between the incident and reflected sheet. Figure b) plots the same results, but zoomed in on the caustic region to demonstrate the differences in fields obtained from the different methods.

where  $r$  is the distance from the beam centre, perpendicular to the direction of propagation,  $\sigma$  is the beam width and  $n_s$  is the Super-Gaussian exponent. All 1-D and 2-D validation problems assume lasers polarised out of the simulation plane along the  $z$  axis. The plasma density profiles are given by,

$$n_e(r) = n_0(d/r)^m, \quad (1.21)$$

where  $n_0/n_{text{cr}} = 1.165$ ,  $d = 343 \times S \mu\text{m}$ ,  $m = 3.78$  and  $S$  changes the scale of the density profile, where  $S = 1$  corresponds to scale lengths from implosions using the full OMEGA laser-energy. These values were obtained from fitting the equation to 1-D Rad-Hydro calculations using the LILAC code.

#### 1.4.3.1 1D Reflected Beam

The first validation problem is for the case of light propagating normally up a density gradient. For this problem, 1-D Cartesian geometry is used, so the density profile is obtained by transforming the spatial coordinate from equation 1.21,  $r \rightarrow x - 36.42 \mu\text{m}$ , and in this problem, the beam is travelling in the  $+\hat{x}$  direction, with  $I_0 = 14 \text{ W/cm}^2$ . Only a single ray was used because the ray trace is completely 1-D. A scale factor of  $S = 1/16$  was used, resulting in a critical surface at  $x \sim 14.14 \mu\text{m}$ . The simulation has bounds  $x \in [-16, 20] \mu\text{m}$  with a resolution of  $\Delta x \sim 1 \text{ nm}$ . A high resolution is used here in order to resolve the highly oscillatory coherent field sum. Power changes of the rays due to inv-Brem and CBET are also neglected.

The laser in this problem travels up the density gradient, reflecting from the critical surface. For normally incident light up a linear gradient, the critical density is the location of the caustic, because the ray area,  $S(\tau)$ , is constant and therefore the amplitude diverges when  $\epsilon \rightarrow 0$ . The total field is given by the coherent sum between the incident and reflected sheets. Figure 1.12.a shows the LPSE result compared to the field obtained from SOLAS without a

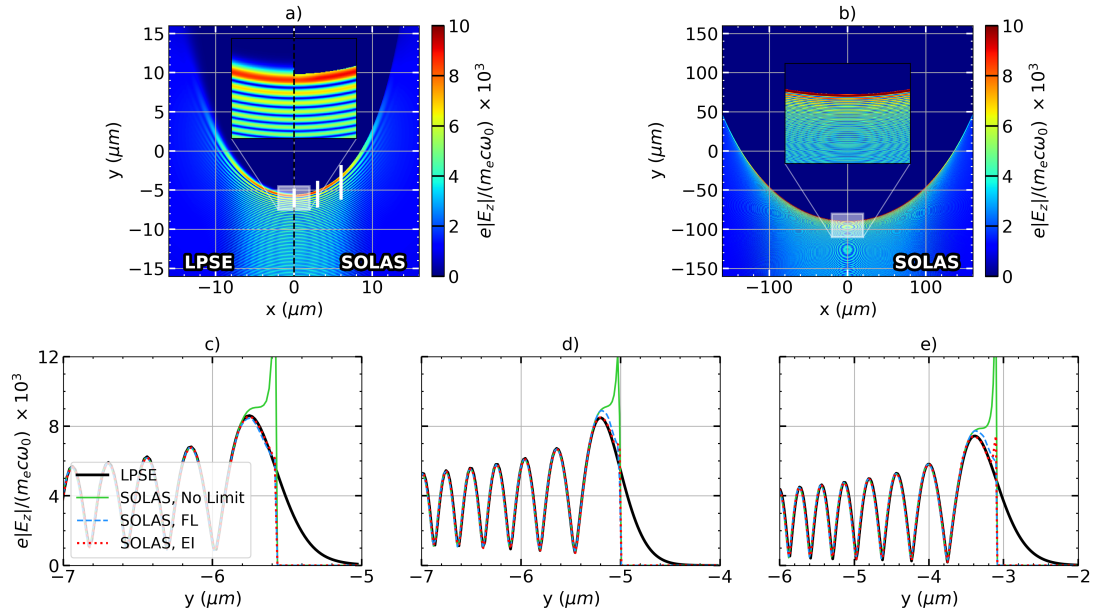


Figure 1.13: This figure shows the results of the 2-D field reconstruction test. Figure a) plots the field from LPSE on the left side and the SOLAS field on the right for the 1/64 OMEGA scale simulation. Figure b) shows the SOLAS field from the 1/4 scale simulation which, when compared to a), demonstrates that as scale increases, the relative size of the caustic region decreases. Figures c), d) & e) are lineouts near the caustic region along  $y$  from the 1/64 scale simulations at  $x = 0, 3 \& 6 \mu\text{m}$  respectively, the positions of which are indicated by the white lines on a). Note that the circular features in the field in figures a) and b) arise due to aliasing artefacts between the true solution scale, with the resolution of the image and, or simulation grid.

cap on the caustic field; using the FL approach; and using the EI approach. The only difference between the SOLAS methods occurs in the caustic region<sup>12</sup>, shown more clearly in figure 1.12.b, which in this problem is for  $x > 13.64 \mu\text{m}$ . Failure to cap the caustic field leads to a divergent  $|E_z|$  at the critical surface, but both the EI and the FL methods show very good agreement with LPSE. This justifies the default use of the simpler FL method for SOLAS CBET calculations.

Standard GO cannot capture the field beyond the critical surface because rays cannot propagate beyond  $\varepsilon = 0$ . The evanescent field in this region can be reproduced in the complex-GO framework, which integrates rays which have complex-valued properties and can thus be evolved beyond the critical surface [19]. This is not deemed to be necessary for accurate CBET modelling of OMEGA-scale direct-drive implosions, however.

#### 1.4.3.2 2D Reflected Beam

A second field reconstruction test was also implemented in 2-D geometry. Unlike the previous 1-D test, the reconstructed field for this problem also depends on the divergence of neighbouring rays. This is because apart from normally incident rays at the centre of the

<sup>12</sup>i.e. where equation 1.19 is satisfied.

beam,  $\mathbf{k} \nparallel \nabla n_e$ , so the area,  $S(\tau)$ , of the rays vary. Simulations at 1/64 and 1/4 scales are presented here. The  $S = 1/64$  simulation had bounds  $x, y \in [-20, 20] \mu\text{m}$  and resolution  $\Delta \sim 20 \text{ nm}$ . The  $S = 1/4$  simulation had bounds  $x, y \in [-200, 200] \mu\text{m}$  and resolution  $\Delta \sim 100 \text{ nm}$ . For both scales, a single beam propagated parallel to  $+\hat{\mathbf{y}}$  and was centred on  $x = 0 \mu\text{m}$ . The beam widths were  $\sigma = 8 \text{ & } 115 \mu\text{m}$  for the 1/64 and 1/4 scales respectively. The standard uniform sampling procedure described in Sec. 1.3.3 was used with  $C_N = 2$ . CBET and inv-Brem were again both neglected.

Figure 1.13.a shows the LPSE and SOLAS, FL fields for the  $S = 1/64$  setup. Agreement appears to be very good by eye between the LPSE and ray-based field in the sub-critical plasma. The field from the SOLAS FL  $S = 1/4$  simulation is plotted in figure 1.13.b, from which it can be seen that the caustic region, which has a characteristic width  $\sim \lambda_0$ , shrinks in relative size as the scale increases. This suggests that at increasing scale, the importance of accurate caustic modelling may decrease in importance. Plotted in figures 1.13.c, 1.13.d & 1.13.e are lineouts from the 1/64 simulations taken at  $x = 0, 3 \text{ & } 6 \mu\text{m}$  respectively. They all include LPSE and SOLAS results with FL, EI caustic field capping along with no limiting. These plots demonstrate that caustic field limiting is necessary to compare favourably to the LPSE solution and that the FL approach slightly overestimates the caustic field compared to LPSE and the EI method. The discrepancy between the FL and EI results is again deemed sufficiently small to justify the default use of the simpler FL approach. To remind the reader, this choice is because the implementation of the EI method in SOLAS requires grid resolution  $\Delta \ll \lambda_0$ , the reason for which is described at the end of Sec. 1.4.2.

## 1.5 Ray Based CBET Model

This section shall describe the implementation of the CBET model in SOLAS. Initially a broad overview of the model shall be provided. Fig. 1.14 shows a flowchart which illustrates the operational loop of the CBET model when coupled to CHIMERA. The initial ‘field reconstruction’ raytrace in the absence of CBET, follows the procedure described in Sec. 1.4 to obtain the field for every beam and sheet on the SOLAS mesh. Ray-based CBET models, including the model in SOLAS, typically must perform repeated ray-traces through the same hydrodynamic profiles to account for pump depletion and optionally energy conservation.

The pump depletion loop, described in more detail in Sec. 1.5.5 is a fixed point iteration method to obtain the new CBET laser fields. This loop is necessary as each iteration produces a new background field which leads to a different CBET interaction, which converges when CBET has been fully accounted for. The resultant solution will not necessarily conserve energy if CBET occurs in the presence of laser caustics. To remedy this, additional energy conservation iterations can be performed, where a multiplier on the CBET gain in caustics can be varied to conserve laser energy. Although this is an ad-hoc correction, it is found to lead to better agreement with higher fidelity solver [29].

CBET does not affect the trajectory of light, just its energy and therefore repeating the calculations of ray trajectories is both computationally costly and unnecessary. Ray locations are therefore stored in a memory-efficient, linked-list to be re-used in both loops. It is found

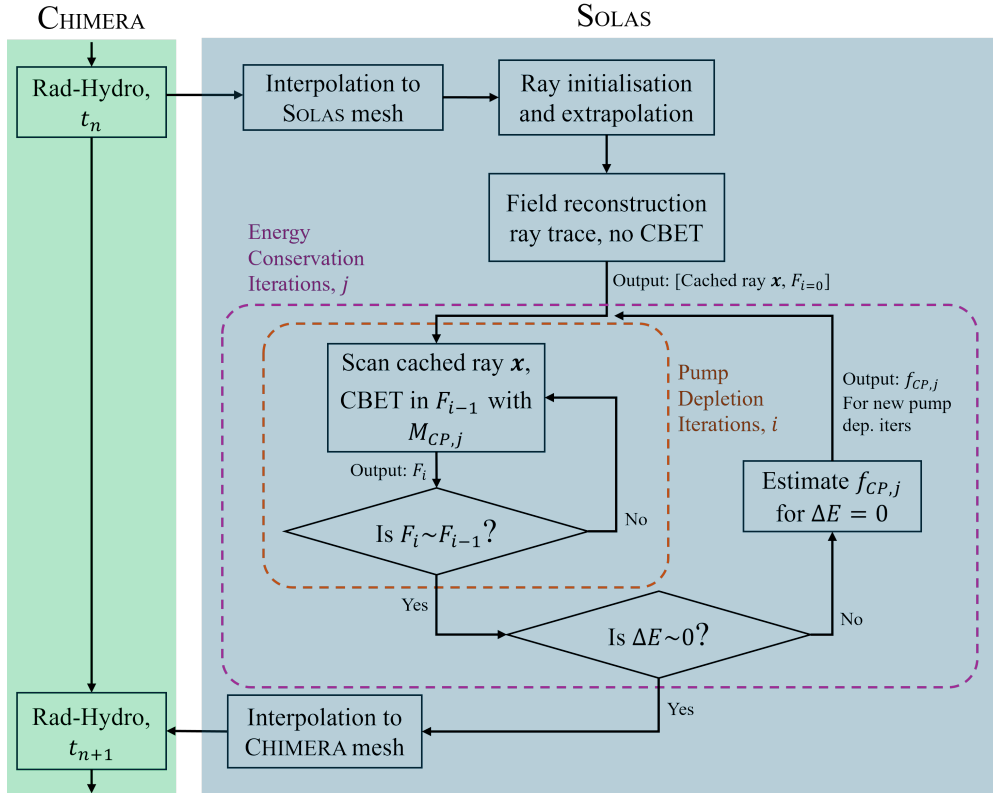


Figure 1.14: A flowchart which illustrates the SOLAS CBET model operation loop.  $F_i$  is short-hand for the total field from all laser beams and sheets at pump depletion iteration  $i$  and  $f_{CP}$  is the modifier to the caustic pump multiplier, described in Sec. 1.5.6 of the  $j^{\text{th}}$  energy conservation iteration.  $\Delta E$  denotes the energy conservation error, which is the total incident power minus deposited power and power exiting the grid.

in SOLAS that caching the ray locations in this manner typically leads to an order of magnitude speed up compared to performing a new raytrace for every iteration.

### 1.5.1 Power Change of Rays due to CBET

Ray-tracing calculations assume steady state hydrodynamic profiles for rays propagating through the plasma and that the field of a ray propagates as a plane wave along the ray path [59]. The linear gain theory of SBS can therefore be used [16], which describes the steady state energy change of locally plane wave light which passes through uniform plasma conditions [10]. Linear in this context means that the plasma response to the driving fields is sufficiently small to be treated in linear expansions. The uniform assumption here means that the plasma conditions must not vary significantly over the interaction time or length scales. For direct-drive conditions, hydrodynamic time scales are typically  $\sim 100\text{ps}$  and CBET saturates on the order of  $\sim 10\text{ps}$ . Ray steps are also limited to grid cell boundaries, which are smaller than hydrodynamic length-scales, so it is safe to assume a locally uniform plasma background when this model is applied only over a single ray step at a time.

The steady-state interaction between two parallel-polarised sheets  $(i, j)$  over a path length

$d\tau$  can be written in terms of the field magnitude of the sheet ( $|E_{i,j}|$ ) or equivalently ray power ( $P_{i,j} = A_{i,j}|E_{i,j}|^2$ ),

$$\begin{aligned}\frac{d|E_i|^2}{d\tau} &= (-\kappa_{IB} + \gamma_{ij}|E_j|^2)|E_i|^2, \\ \frac{dP_i}{d\tau} &= (-\kappa_{IB} + \gamma_{ij}A_jP_j)P_i,\end{aligned}\quad (1.22)$$

where  $\kappa_{IB}$  is the inv-Brem absorption kernel,  $A_j$  is the amplitude of sheet  $j$  and  $\gamma_{ij}$  is the CBET gain of sheet  $i$  from the interaction with sheet  $j$ . The sheet/ray which changes energy in a given interaction (here  $i$ ), is often called the *probe* while the other beam is termed the *pump*. The gain is a function of both the plasma conditions and the local field profiles for both sheets in the interaction, so a gain must be calculated between every pair of sheets at every location where both are present. Going from the first to the second equation assumes that  $dA_i/d\tau = 0$ , which is consistent with the assumption from the linear gain theory that the fields are approximately uniform over a small step. Different models exist for the gain, which either use a fluid or kinetic treatment for the plasma IAW response.

When multiple different probe beams are present, the total CBET interaction is treated simply as the sum of all interactions from different sheets,

$$\frac{dP_i}{d\tau} = (-\kappa_{IB} + \kappa_{CBET})P_i, \quad (1.23)$$

where the CBET kernel has been defined  $\kappa_{CBET} = \sum_{j \neq i} \gamma_{ij}|E_j|^2$ . This summation assumes that the fields from different sheets are uncorrelated. For direct-drive conditions, this assumption is broadly correct, apart from when a probe sheet undergoes a CBET interaction in the caustic region of the probe. In this case, the *Coherent Caustic* correction is applied, which is described in Sec. 1.5.3.

Note that when computing both inv-Brem and CBET, the partition of power lost to each interaction is computed as,

$$\begin{aligned}\Delta P_{i,IB} &= -\langle P_i \rangle \frac{\kappa_{IB}}{\kappa_{CBET} - \kappa_{IB}}, \\ \Delta P_{i,CBET} &= \langle P_i \rangle \frac{\kappa_{CBET}}{\kappa_{CBET} - \kappa_{IB}}, \\ \langle P_i \rangle &= P_i + P_i(\kappa_{CBET} - \kappa_{IB})d\tau/2,\end{aligned}\quad (1.24)$$

where  $\Delta P_{i,IB}$  and  $\Delta P_{i,CBET}$  are the powers lost to inv-Brem and CBET respectively and  $\langle P_i \rangle$  is the average power of the ray over the step,  $d\tau$ . This can be derived by solving Eq. 1.22 for  $P_i$  and then taking the limit  $d\tau \rightarrow 0$  [23]. The deposition,  $\Delta P_{i,IB}$ , can then be interpolated to the grid as an electron energy source as is described in Sec. 1.3.4.

The two formulations of the gain shall be presented below. Broadly, the gain describes the plasma response to the 2 driving fields and therefore dictates the energy transfer between them. They differ in that the fluid formulation derives a gain by linearising the fluid equations for the plasma response whereas the kinetic formulation is obtained from a linearisation of the Vlasov equation. The kinetic gain is more complete and should be used for comparison to experimental observables, whereas the fluid gain is useful for comparison

with LPSE, which directly solves the linearised fluid equations.

**Fluid CBET Gain** The linear fluid gain, described by Randall *et al.* in Ref. [16] is,

$$\begin{aligned}\gamma_{ij} &= \frac{n_e e}{4m_e c \omega_i} \frac{1}{T_e (1 + 3T_i/ZT_e)} \frac{R(\eta_{ij})}{\nu_{ia}}, \\ R(\eta_{ij}) &= \frac{(\nu_{ia}/\omega_s)^2 \eta_{ij}}{(\eta^2 - 1)^2 + (\nu_{ia}/\omega_s)^2 \eta_{ij}^2}, \\ \eta_{ij} &= \frac{(\omega_j - \omega_i) - \mathbf{k}_s \cdot \mathbf{u}}{\omega_s},\end{aligned}\quad (1.25)$$

where  $T_e$  &  $T_i$  are the electron & ion temperatures in eV respectively,  $\omega_i$  &  $\mathbf{k}_i$  are the frequency and wavevector of sheet  $i$  respectively,  $Z$  is the ionisation state,  $\mathbf{u}$  is the fluid velocity,  $\omega_s = |\mathbf{k}_s|c_s$  is the IAW frequency,  $\mathbf{k}_s = \mathbf{k}_j - \mathbf{k}_i$  is the IAW wavevector,  $c_s = \sqrt{e(ZT_e + 3T_i)/m_i}$  is the sound speed and  $\nu_{ia}$  is the IAW damping rate. This formulation is useful for comparison with LPSE, which directly solves the linearised fluid equations and therefore in situations where the GO assumptions are valid, the two methods should give similar results. However, it is generally not considered to be a good choice of model to compare to experiment. The damping rate,  $\nu_{ia}$  does not have an analytic formula for arbitrary plasma conditions and therefore must be prescribed. Additionally, Eq. 1.25 assumes an average ion treatment of the species in the plasma if multiple ion species are present. In reality, both fast and slow modes of IAW can be driven in a 2 species plasma [60], which can independently lead to CBET scattering. This effect cannot be captured using the fluid gain, where the plasma is assumed to be made of a single ion species with a number density averaged ion mass. Codes that use this formulation typically use a damping value  $\nu_{ia}/\omega_s = 0.2$  for CH plasmas, which is the value used for all fluid gain simulations in this chapter.

**Kinetic CBET Gain** The linear kinetic CBET gain, described by Michel in Ref. [61] is,

$$\begin{aligned}\gamma_{ij} &= \frac{e^2 |\mathbf{k}_s|^2}{4m_e^2 c \omega_i^3} \text{Im}(K_{ij}), \\ K_{ij} &= \frac{\chi_e(1 + \chi_i)}{(1 + \chi_e + \chi_i)}, \\ \chi_e &= \frac{-1}{2|\mathbf{k}_s|^2 \lambda_{De}^2} Z' \left( \frac{(\omega_j - \omega_i) - \mathbf{k}_s \cdot \mathbf{u}}{\sqrt{2} |\mathbf{k}_s| v_{Te}} \right), \\ \chi_i &= \frac{-1}{2|\mathbf{k}_s|^2 \lambda_{De}^2} \frac{T_e}{\langle Z \rangle T_i} \sum_{\alpha}^{\text{species}} f_{\alpha} Z_{\alpha}^2 Z' \left( \frac{(\omega_j - \omega_i) - \mathbf{k}_s \cdot \mathbf{u}}{\sqrt{2} |\mathbf{k}_s| v_{T\alpha}} \right),\end{aligned}\quad (1.26)$$

where  $\chi_e$  &  $\chi_i$  are the electron & ion susceptibilities respectively,  $f_{\alpha}$  &  $Z_{\alpha}$  are the number fraction & ionisation of ion species  $\alpha$  respectively,  $Z'$  is the derivative of the plasma dispersion function,  $v_{Tn} = \sqrt{eT_n/m_n}$  is the thermal velocity of species  $n$  with temperature  $T_n$  in eV and mass  $m_n$ ,  $\lambda_{De} = \sqrt{\epsilon_0 e T_e / n_e e^2}$  is the electron Debye length and  $\langle Z \rangle = \sum_{\alpha} f_{\alpha} Z_{\alpha}$  is the average ionisation. Note that the susceptibilities  $\chi_{i,e}$  are complex, which arises from the complex plasma dispersion function. In order to compute  $Z'$  in SOLAS, the CALGO library

is used to numerically compute the value of the *Faddeeva function*,  $w(x)$  [62]. This is then related to the plasma dispersion function and its derivative by,

$$\begin{aligned} Z(x) &= i\sqrt{\pi}w(x), \\ Z'(x) &= -2[1 + xZ(x)], \end{aligned} \tag{1.27}$$

where  $i = \sqrt{-1}$  and  $w(x)$ ,  $Z(x)$  and  $Z'(x)$  are all complex numbers [63]. Unlike the fluid gain, this correctly captures the resonance and has no effective free parameters, making it the judicious choice for predictive simulations. The plasma dispersion function is however relatively slow to numerically evaluate and dominates computational runtime if evaluated every ray step. SOLAS therefore calculates  $\gamma_{ij}$  between each sheet in every grid cell at the end of the field reconstruction ray trace (from Fig. 1.14) and then interpolates this pre-calculated value onto the ray locations for the pump-depletion iterations. This reduces computational runtimes by orders of magnitude for many beam direct-drive simulations, but has an associated memory overhead, which is discussed in more detail in Sec. 1.5.4. All simulations in this thesis use the kinetic CBET gain unless explicitly stated otherwise.

**Random Polarisation Correction** The gains calculated above all assume that the interacting fields have parallel polarisations. For many laser systems, beams may have arbitrary or random polarisations, such as at the OMEGA laser facility where Distributed polarization rotators (DPRs) separate each beam into 2 orthogonally polarised sub-beams which overlap to effectively have one spot with random polarisation [64]. If a simulation is conducted with multiple beams of random polarisation, a *Polarisation Smoothing* multiplier,  $M_{PS}$ , must be applied to the value of  $\gamma_{12}$  which accounts for random polarisation angles between the field from different sheets,

$$M_{PS} = \frac{1}{4}(1 + \cos^2 \theta), \tag{1.28}$$

where  $\theta$  is the angle between the wavevectors of the interacting sheets.

#### MAYBE TRANSFER BELOW TO THEORY SECTION!

In reality, the DPRs on OMEGA do not actually create a single, mixed polarisation laser spot, but 2 slightly offset sub-beams on the target. CBET models which track polarisation or rays have been developed which account for the true polarisation angle between 2 sheets [65–68]. These models have demonstrated that polarised CBET on OMEGA creates a mode-1 which is always in the same direction. This persistent mode-1 was experimentally observed from neutron time of flight diagnostics before its origin was understood [69].

### 1.5.2 Caustic Gain Truncation

For rays propagating through SOLAS cells, nearest neighbour interpolation is used to interpolate field quantities to the rays. This is generally an adequate approximation for field magnitudes, frequencies and wavevectors, which vary over greater length scales than typical cell resolutions  $\mathcal{O}(1\mu\text{m})$ , apart from in the vicinity of a caustic [29]. Near caustics, rays turn sharply and fields have a very sharp *cut off* as be seen for example in Fig. 1.13. The sharp

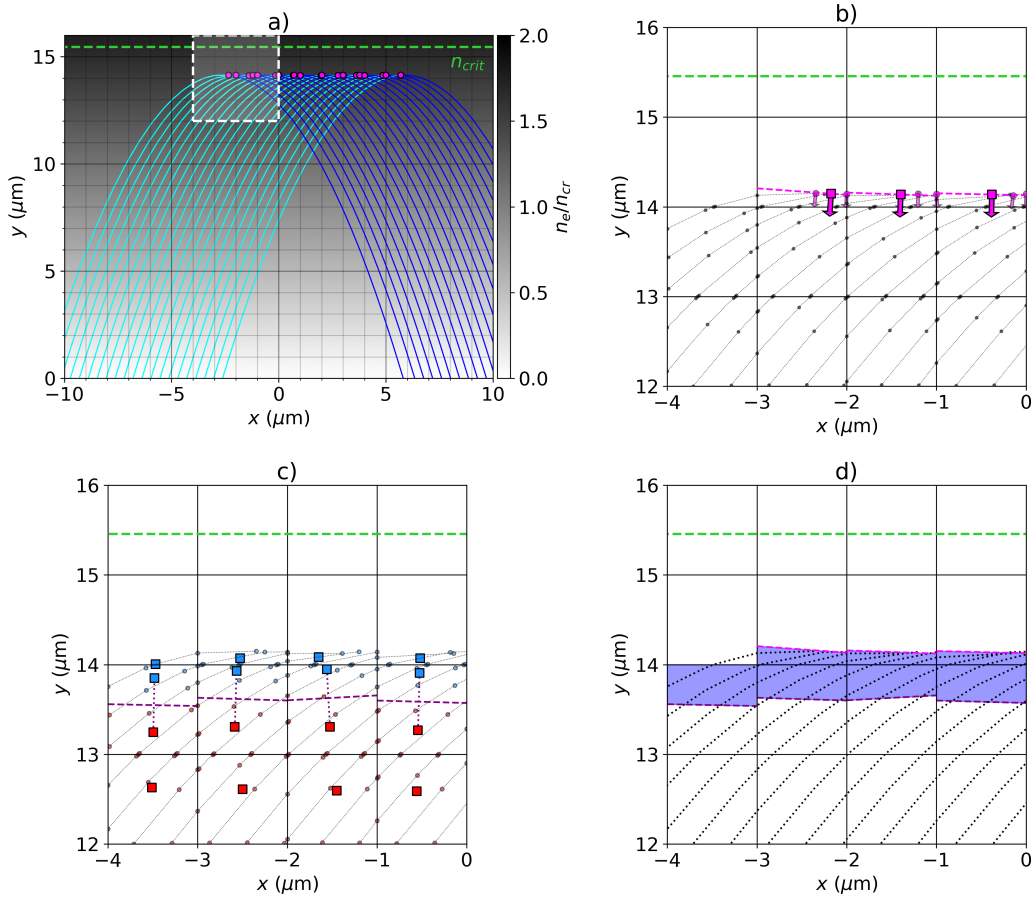


Figure 1.15: A series of figures which illustrate how the caustic region identification in SOLAS work. Figure a) shows a laser, separated into incident and reflected sheets by a caustic, propagating up and reflecting in a linear density ramp. Caustic Gain Truncation (CGT) is illustrated in b) where a cell is separated into a *lit* and *unlit* region by the reconstructed *caustic plane*. Figures c) and d) illustrate the method used to identify the *caustic region*, where the coherent caustic modifier is applied. c) shows that cells are geometrically separated into *capped* and *uncapped* regions and the coherent caustic modifier to the gain is applied in this capped region.

turning of rays mean that  $\mathbf{k}$  can vary rapidly within a cell. Although SOLAS does have variable radial resolution, as described in Sec. 1.4, this resolution is limited to the minimum radial cell size from the hydrodynamic grid, which is not dictated from laser parameters and cells are typically larger than the caustic region width  $\mathcal{O}(\lambda_0)$ . The issue of  $\mathbf{k}$  variation is not addressed in SOLAS, but linear interpolation or a truly adaptive mesh, separate from the CHIMERA grid could be implemented to address this.

The field cut off is a significant issue however, which can significantly affect energy conservation in ray based CBET models. CGT is an algorithm that effectively improves the resolution of the grid near laser caustics [28]. This method separates cells into *lit* and *unlit* regions. If rays travel in the *unlit* region, then the CBET gain is not applied. For example, Fig. 1.15.a shows a beam propagating up a linear density gradient, separated by the caustic into inci-

dent and reflected sheets. Fig. 1.15.b shows a zoomed in view of in the vicinity of the caustic of the incident sheet ray locations, plotted as grey dots. If a ray from another beam were present with  $14.3 \lesssim y < 15 \mu\text{m}$ , nearest neighbour interpolation would lead to ray undergoing a CBET interaction occurring in this *unlit* region, where no rays from the pump sheet are present. Field magnitudes in this caustic region are typically large, so even though this is a small region of space, it can lead to significant errors, especially at lower resolutions.

The CGT algorithm described by Follett in Ref. [28] defines the *lit* region for each sheet by creating a mesh of the caustic locations from every ray on the sheet and only applying CBET gains in on the side of this mesh that rays traversed. A different algorithm has been developed for SOLAS, which geometrically splits each cell into *lit* and *unlit* regions by a *caustic plane* if at least one ray caustic occurs in the cell. The *caustic plane*<sup>13</sup> is defined by a point  $\mathbf{x}_{\text{caus}}$  and normal  $\hat{\mathbf{n}}_{\text{caus}}$ . The location,  $\mathbf{vecx}_{\text{caus}}$ , is simply the average of all ray caustic locations from the sheet present in the cell, for example shown in Fig. 1.15.b by the small pink circles for each ray caustic and the larger pink square for the cell averaged location. The normal is estimated by the average over all ray caustics in the cell of the ray tangent vector just after the caustic  $\hat{\mathbf{t}}_{\text{After}}$ , minus the velocity just before  $\hat{\mathbf{t}}_{\text{Before}}$ ,

$$\hat{\mathbf{n}}_{\text{caus}} = \left\langle \frac{\hat{\mathbf{t}}_{\text{After}} - \hat{\mathbf{t}}_{\text{Before}}}{|\hat{\mathbf{t}}_{\text{After}} - \hat{\mathbf{t}}_{\text{Before}}|} \right\rangle, \quad (1.29)$$

such that the normal points to the lit side. This is plotted in Fig. 1.15.b as small pink arrows for each ray caustic normal and the large arrows in each cell for the cell averaged value. The planes defined by these points and normals for each cell that contains a sheet caustic is shown as a pink dashed line. If a probe ray at location  $\mathbf{x}_{\text{probe}}$  is propagating in a cell where there is a pump sheet caustic, it will only experience a CBET interaction if  $\hat{\mathbf{n}}_{\text{caus}}(\mathbf{x}_{\text{probe}} - \mathbf{x}_{\text{caus}}) > 0$ . Rays from other sheets also have their steps limited by the caustic plane.

This is a slightly lower fidelity implementation of the more complete CGT model in Ref. [28], which can represent caustics which, within a grid cell, are not locally well approximated by planes. It is however simpler to implement and does act to effectively increase the resolution of the cells near caustics. The caustic test problem presented in Sec. 1.5.7.2 illustrates the effectiveness of the SOLAS-CGT model at reducing energy conservation errors for caustic CBET interactions where the grid cells are significantly larger than the caustic region.

### 1.5.3 Coherent Caustic Correction and Caustic Region Identification

In Sec. 1.5.1, in order to obtain Eq. 1.23, it was assumed that when a ray in undergoing CBET interactions with multiple pump sheets, that the field from the pump sheets can be treated independently. This is equivalent to assuming that over a ray propagation path,  $d\tau$ , the fields from the sheets do not add coherently,

$$\int d\tau \sum_j^{\text{sheets}} |E_j|^2 \approx \int d\tau \left| \sum_j^{\text{sheets}} E_j \right|^2, \quad (1.30)$$

---

<sup>13</sup>In cylindrical and spherical simulation geometries, the ‘planes’ are defined in the native coordinate system, which creates manifolds that better reflect the assumed geometry of the problem.

where  $E_j$  is the field from the  $j^{\text{th}}$  sheet, which is valid for all regions of space where the phase from different sheets are uncorrelated. For direct-drive configurations, this assumption holds everywhere apart from the caustic region of the pump sheet, where fields add coherently. Thus, the coherent sum of fields in the caustic region is larger than the incoherent sum, so without correcting for this, CBET scattering through a pump beam in its caustic region will be underestimated.

The ratio of the coherent and incoherent sums of incident ( $E_{\text{inc}}$ ) and reflected ( $E_{\text{refl}}$ ) fields of the pump sheet in its caustic region is called the *coherent caustic multiplier*,

$$M_{\text{CP}} = \frac{|E_{\text{inc}}|e^{i\phi_{\text{inc}}} + |E_{\text{refl}}|e^{i\phi_{\text{refl}}}}{|E_{\text{inc}}|^2 + |E_{\text{refl}}|^2}. \quad (1.31)$$

By making the same assumption as used to obtain Eq. 1.18, that  $|E_{\text{inc}}| \sim |E_{\text{refl}}|$ , this simplifies to,

$$M_{\text{CP}} = 1 + \sin(\phi_{\text{refl}} - \phi_{\text{inc}}), \quad (1.32)$$

which should be applied in the caustic region, as defined in Eq. 1.19, where  $|\varphi_1 - \varphi_2| \leq \lambda_0/2$ . As stated in the discussion in Sec. 1.4.2, grid cells are typically larger than the size of the caustic region ( $\mathcal{O}(\lambda_0)$ ) and SOLAS does not include linear interpolation of field quantities. Therefore, Eq. 1.32 cannot robustly be evaluated at the relevant scales. The caustic region is identified by geometric a geometric algorithm, similar to the *caustic plane* method discussed in Sec. 1.5.2 and the average value of the coherent caustic multiplier is used,

$$M_{\text{CP}} = 1 + 2/\pi, \quad (1.33)$$

when a ray undergoes CBET with a pump sheet in its caustic region. This coherent caustic correction increases the CBET scattering and is an important addition to make sure that CBET models are energy conserving.

As stated above, SOLAS does not employ linear interpolation of phases and therefore to estimate when a ray is in the caustic region of another beam,  $|\varphi_1 - \varphi_2| \leq \lambda_0/2$ , an alternative algorithm has been developed. Similarly to the *caustic plane* method from Sec. 1.5.2, this algorithm works by finding planes that separate cells to increase the resolution of cells which use nearest neighbour interpolation of fields. The key assumptions of the method are that the boundary of the caustic region can be treated locally in grid cells as a plane and that the caustic region is approximately where ray amplitudes are greater than the FL capped amplitude,  $A_{\text{ray}} > A_{\text{FL}}$ . Fig. 1.15.c plots the trajectory of incident sheet rays from Fig. 1.15.a, with the locations of capped & uncapped rays plotted as small transparent red & blue dots respectively. The average value of each of these locations is represented by the larger blue ( $\langle \mathbf{x}_{\text{cap}} \rangle$ ) and red squares ( $\langle \mathbf{x}_{\text{uncap}} \rangle$ ) respectively, which is stored, where present, in each SOLAS grid cell. The region of the cell occupied by these capped (blue) ray locations is assumed to be equivalent to the caustic region. The validity of the assumption was tested by conducting high resolution simulations of the 2-D reflected beam field reconstruction test in Sec. 1.4.3 to accurately reconstruct the phase and amplitudes of incident and reflected sheets on a high resolution mesh. It was found that the assumption is adequate, although it typically

slightly overestimates the width of the caustic region by  $\mathcal{O}(10\%)$ . This is not considered to be a significant issue, because energy conservation iterations are employed which minimise errors by varying  $M_{\text{CP}}$  over multiple iterations. Therefore, errors in the initial iteration are compensated by this minimisation.

To geometrically estimate the caustic region in cells which contain both capped (blue) and uncapped (red) ray locations, a *caustic region plane* is defined to separate these regions, defined by a point,  $\mathbf{x}_{\text{CR}}$ , and normal,  $\hat{\mathbf{n}}_{\text{CR}}$ ,

$$\begin{aligned}\mathbf{x}_{\text{CR}} &= \frac{\langle \mathbf{x}_{\text{cap}} \rangle + \langle \mathbf{x}_{\text{uncap}} \rangle}{2}, \\ \hat{\mathbf{n}}_{\text{CR}} &= \frac{\langle \mathbf{x}_{\text{cap}} \rangle - \langle \mathbf{x}_{\text{uncap}} \rangle}{|\langle \mathbf{x}_{\text{cap}} \rangle - \langle \mathbf{x}_{\text{uncap}} \rangle|},\end{aligned}\quad (1.34)$$

where  $\hat{\mathbf{n}}_{\text{CR}}$  is defined such that it points toward to caustic region. For a probe ray propagating through a mesh which contains a pump field, the ray is inside the caustic region if  $\hat{\mathbf{n}}_{\text{CR}} \cdot (\mathbf{x}_{\text{probe}} - \mathbf{x}_{\text{CR}}) > 0$ , under which circumstances, the pump-probe CBET gain is multiplied by the average value of  $M_{\text{CP}}$  defined in 1.33. This is illustrated in Fig. 1.15.c by the purple dashed lines. If a cell contains both a *caustic region plane* and a *caustic plane* (from Sec. 1.5.2), then the ray must be inside the caustic and on the lit side of the caustic to undergo CBET with  $M_{\text{CP}}$  applied. Fig. 1.15.d plots the caustic region, as obtained by the algorithm, as a transparent blue shaded area.

#### 1.5.4 Dynamic Memory for Storing Fields and CBET Gains

CBET gains must be calculated between every pair of sheets that cross at a given location. For  $N_b$  beams, each with 2 possible sheets, discretised on a grid with  $N_x$  cells in each dimension, a total of  $N_f \sim 2N_x^3 N_b$  *field data points* must be stored. Each of these data points must store the field magnitude, phase, wavevector and information used to evaluate CGT and the coherent caustic correction where necessary, as described in Sec. 1.5.2 and 1.5.3 respectively. This amounts to large computational memory requirements to store the fields. Additionally, SOLAS stores the CBET gains between each laser sheet to improve the code execution time. A separate gain exists between each sheet and therefore the memory cost to store this information scales as  $N_g \sim 2N_f^3 N_b^2$ .

$N_g$  is a single number and  $N_f$  represents all field information, so for simulations with small numbers of beams,  $N_f$  is the dominant memory cost, whereas for large number of overlapping beams such as direct-drive simulations,  $N_g$  dominates. It is therefore important to use a memory efficient method to store this data so that large scale, 3-D simulations can be completed. SOLAS utilises pointers in each grid cell to dynamically allocate the field data, such that only where a sheet is present is its corresponding field magnitude, phase *etc.* stored. Additionally, gains between sheets are an attribute of the field data and are stored as single-precision floats, rather than the native SOLAS double precision, which also reduces memory costs for large simulations. These measures significantly reduces memory overhead for multidimensional CBET simulations, however high resolution 3-D simulations are still extremely memory intensive, which is an issue also experienced by IFRIIT, the other 3-D CBET

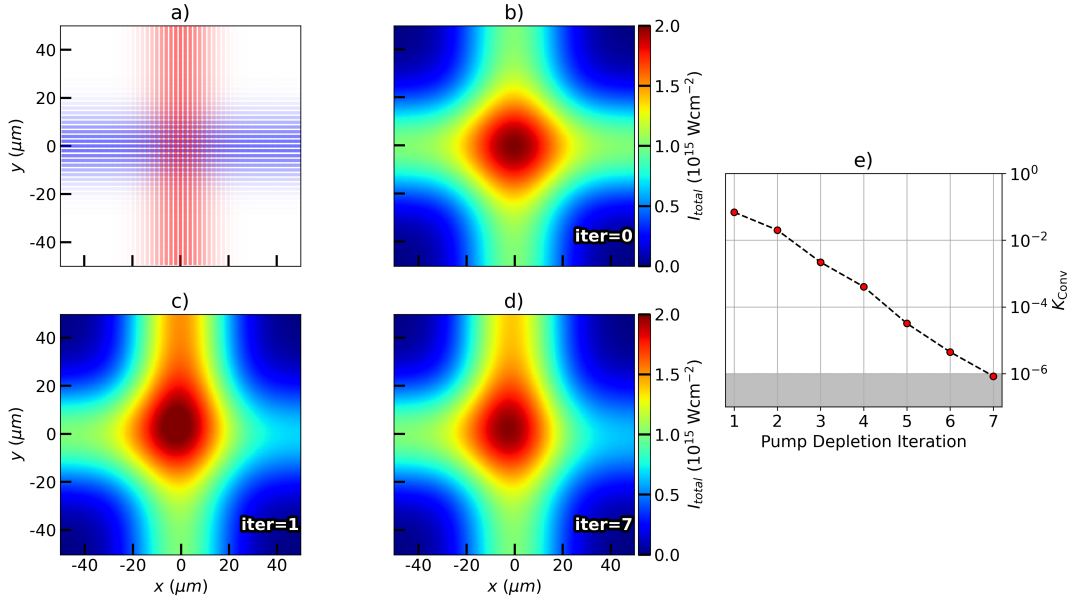


Figure 1.16: This figure shows the results of successive pump depletion iterations for an illustrative simulation of 2 beams crossing and undergoing a CBET resonance in a uniform plasma background. Each beams' rays from the field reconstruction ray trace are plotted in a), where more opaque rays indicate a higher power. Panel b) plots the reconstructed intensity from this ray trace, where  $i = 0$  indicates the field reconstruction ray trace and therefore no CBET occurs. Panels c) & d) plot the intensity reconstructed from the 1<sup>st</sup> & 7<sup>th</sup> pump depletion iterations, where the effect of transfer of powers between beams due to CBET is evident. Panel e) plots the convergence parameter from the simulation over successive pump depletion iterations, with convergence defined here as  $K_{\text{Conv},0} = 10^{-6}$ .

code coupled to hydrodynamics.

### 1.5.5 Pump Depletion Iterations

The field reconstruction ray trace (the initial ray trace performed in the absence of CBET) returns the field from each sheet  $|E_j^{i=0}|(\mathbf{x}, \mathbf{k}, \omega, \phi)$ , where  $j$  is the sheet index and  $i = 0$  indicates the field reconstruction ray trace. This field is discretised on the SOLAS mesh using nearest neighbour interpolation, so that a ray passing through a cell updates the field in that cell. Rays can then be re-traced through this mesh and undergo changes in power due to CBET interactions with the fields from other sheets. The solution obtained from a single raytrace with CBET is not the true solution however, because the field that the rays see throughout the CBET raytrace is not dynamically updated by the change in ray power due to CBET as they propagate. This necessitates iteratively solving the ray trace to account for CBET, whereby for iteration  $i$ , the rays from sheet  $j$  propagate through the mesh and undergo CBET through  $|E_{\text{sheet} \neq j}^{i-1}|$ , while building up a new field,  $|\tilde{E}_j^i|$ . The new fields *build-up*,  $|\tilde{E}_j^i|$ , are introduced for the next iteration. This loop is repeated until convergence of the field has been achieved. Convergence is tested each iteration ( $i > 0$ ) against the total power of rays  $\tilde{P}_{j,n}^i$ , from each

sheet  $j$  travelling through each cell, explicitly defined by the convergence parameter,

$$K_{\text{Conv}}^i = \max_{\substack{j \in \text{sheets} \\ n \in \text{cells}}} \left| \left( \tilde{P}_{j,n}^i / \tilde{P}_{j,n}^{i-1} \right) - 1 \right| < K_{\text{Conv},0}, \quad (1.35)$$

where  $K_{\text{Conv},0}$  is a user defined parameter, typically set to  $10^{-5}$  unless stated otherwise.

This procedure is illustrated in Fig. 1.16 for a simple, illustrative problem of 2 beams crossing in a uniform, stationary plasma background with a frequency difference between the beams tuned to give a CBET resonance. The effect of inv-Brem deposition has been neglected in this simulation. Fig 1.16.a shows the ray trajectories for the two crossing beams and Fig. 1.16.b plots the intensity from the field reconstruction iteration, without CBET. The intensities after one & 7 pump depletion iterations are plotted in Fig. 1.16.c & Fig. 1.16.d respectively, which show that a single re-trace through the no-CBET fields does not return the converged solution. Fig 1.16.e plots the convergence parameter after each iteration, illustrating that 7 iterations was required to obtain the converged solution, plotted in Fig 1.16.d.

For many beam simulations with complicated beam trajectories and many overlapping crossings such as direct-drive calculations, the problem is asymptotically unstable. This means that for iteration  $i$ , allowing rays to undergo CBET in the full  $|\tilde{E}_{\text{sheet} \neq j}^{i-1}|$  causes unbounded gains on ray powers leading to divergent results for  $|E_j^i|$ . Numerical damping is therefore applied for these caluclations to stabilise the solution. The actual fields that a ray will see for the subsequent iteration,  $i + 1$ , are composed of the weighted sum of the two *build-up* fields,

$$|E_j^i| = f_{\text{damp}} |\tilde{E}_j^i| + (1 - f_{\text{damp}}) |\tilde{E}_j^{i-1}|, \quad (1.36)$$

where  $f_{\text{damp}}$  is a user-defined damping value, which is by default set to a (relatively conservative) value of 0.75, to ensure that the solver does not diverge for complex problems.

### 1.5.6 Energy Conservation Iterations

The converged field solution from the pump depletion iterations returns the steady state field and deposition profiles, accounting for CBET, given a field reconstruction algorithm, interpolation scheme *etc*. If there are errors in, for example the field reconstruction algorithm, then the pump depletion iterations will return a steady state solution, however this is not guaranteed to be the ‘true’ solution, or the same as obtained by a higher fidelity solver. The main cause of errors in field reconstruction is the treatment of laser caustics, as demonstrated for example in Fig. 1.13. This figure demonstrates that the SOLAS field reconstruction algorithm obtains essentially perfect agreement with LPSE everywhere apart from in the vicinity of the caustic. It can therefore be assumed that any errors in the CBET profiles, returned from the pump depletion iterations, occur due to errors in the field reconstruction and CBET scattering in the caustic region. The energy conservation error,  $\Delta E$ , is a good proxy for the accuracy of the fields obtained from CBET, as in the absence of laser caustics, energy

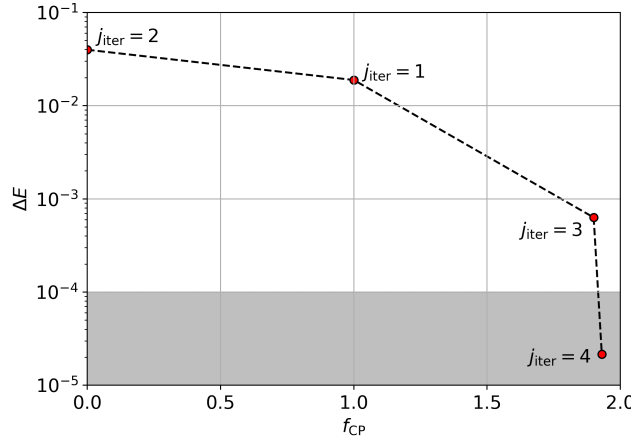


Figure 1.17: This figure shows the results of the energy conservation iterations for a 2 beam caustic test problem, which is presented in Sec. 1.5.7.2. 4 iterations were required to achieve energy conservation, which was defined to be  $\delta E < 1 \times 10^{-4}$ . The order of the iterations is indicated by the text next to each point.

is conserved in ray-based algorithms [29]. This is defined as,

$$\Delta E = \frac{P_{dep} + P_{out} - P_{inc}}{P_{inc}}, \quad (1.37)$$

where  $P_{dep}$ ,  $P_{out}$  and  $P_{inc}$  are the power deposited by inv-Brem, the ray-power leaving the domain and the incident power respectively. If this value is not small, it suggests that caustics are not accurately treated in the CBET scattering.

As in the BEAMCROSSER code, the assumption in SOLAS is made that minimising the  $\Delta E$  by altering the CBET gains in the caustic region will account for bringing the result into better agreement with the true solution [29].  $M_{CP}$  is modified to include a new *caustic pump multiplier*,  $f_{CP}$ , which is applied to probe ray CBET gains, when they are in the caustic region of the pump sheet,

$$\tilde{M}_{CP} = \begin{cases} 1 + f_{CP} \left( \frac{2}{\pi} \right), & \text{if in caustic region} \\ 1, & \text{otherwise} \end{cases} \quad (1.38)$$

where the same, geometric identification for the pump sheet caustic region is used as in Sec. 1.5.3.  $f_{CP} = 1$  initially and is varied between  $f_{CP} \in [-\pi/2, 2]$  over several *energy conservation* iterations<sup>14</sup> to minimise  $\Delta E$ . The lower bound on  $f_{CP}$  is to prevent ‘negative scattering’ in the caustic region, where the sign of the gain flips. The upper bound was selected by experimentation to prevent excessively large gains which result in the exponential power gain of rays blowing up to infinity.

An implementation of the Secant method is used to estimate the next value of  $f_{CP}$ . The first & second energy conservation iterations in a simulation use  $f_{CP} = 1$  & 0, to obtain a gradient with which to estimate values of the multiplier. The Secant method was chosen for its simplicity and the fact that bracketing values of the root are not required. An example of the

<sup>14</sup>Each energy conservation iteration contains a new set of pump depletion iterations, as is shown in Fig. 1.14.

minimisation results are shown in figure 1.17. These results are from a 2 beam caustic test problem, presented in Sec. 1.5.7.2, but the specifics of the problem are not important for the discussion here, simply that CBET in the presence of a caustic occurs. Therefore a caustic region exists inside which  $f_{\text{CP}}$  will lead to modified gains which reduce energy conservation errors. The curve of  $\Delta E(f_{\text{CP}})$  is simple and monotonic, which is observed for all simulations conducted with SOLAS, regardless of the complexity of the laser and target configuration. This means a complex algorithm than the Secant method is not required for minimisation. When the CBET model runs in-line with the hydrodynamics, the value of  $f_{\text{CP}}$  from the previous timestep when CBET was calculated is used which means that energy conservation iterations frequently do not occur. This is shown explicitly in Fig. 1.23, where shows the results of a 1-D CHIMERA-SOLAS simulation of OMEGA shot 89224. The bottom panel in the figure shows that energy conservation is frequently achieved by simply resuing the value of  $f_{\text{CP}}$  from the previous timestep.

To summarise, the total CBET gain that a probe ray ( $i$ ) experiences in a pump sheet ( $j$ ) is,

$$\tilde{\gamma}_{ij} = \gamma_{ij} M_{\text{PS}} \tilde{M}_{\text{CP}}, \quad (1.39)$$

where  $\gamma_{ij}$  is the value defined in Sec. 1.5.1 (depending on if using the kinetic or fluid gain model), the modified coherent caustic multiplier  $\tilde{M}_{\text{CP}}$  is defined in Eq. 1.38 and the polarisation smoothing multiplier,  $M_{\text{PS}}$ , defined in Eq. 1.28, is applied if the beams are assumed to be randomly rather than parallel-polarised.

### 1.5.7 CBET Validation

This section shall present results from several CBET test problems where the results from SOLAS are compared to the wave based solver LPSE. Because comparisons are to LPSE which is a wave-solver coupled to a linearised fluid response, the fluid CBET gain is used for all simulations in this section. Beams in the simulations all have a vacuum wavelength,  $\lambda_0 = 0.351$  nm and a supergaussian spot profile, which was defined in Eq. 1.1. For consistency with LPSE, the Doppler shift of laser frequency is not calucated in these simulations so its effect on CBET is neglected, *i.e.* the right hand side of Eq. 1.5 is forced to be zero. The plasma backgrounds for all initialisations are fully-ionised CH with  $Z = 3.1$  and  $T_i = T_e/2$ . All tests are presented in Ref. [29] and the LPSE data is available from the repository [58].

#### 1.5.7.1 2-D CBET Without Caustics

Table 1.1: The ratio of the power of the seed beam as it exits the domain to its intial power.

	$P_{\text{seed,out}}^{\text{LPSE}} / P_{\text{seed,in}}^{\text{LPSE}}$	$P_{\text{seed,out}}^{\text{BEAMCROSSER}} / P_{\text{seed,in}}^{\text{BEAMCROSSER}}$	$P_{\text{seed,out}}^{\text{SOLAS}} / P_{\text{seed,in}}^{\text{SOLAS}}$
CBET + Absorption	1.315	1.325	1.320
CBET only	1.551	1.561	1.558
Absorption only	0.856	0.856	0.852

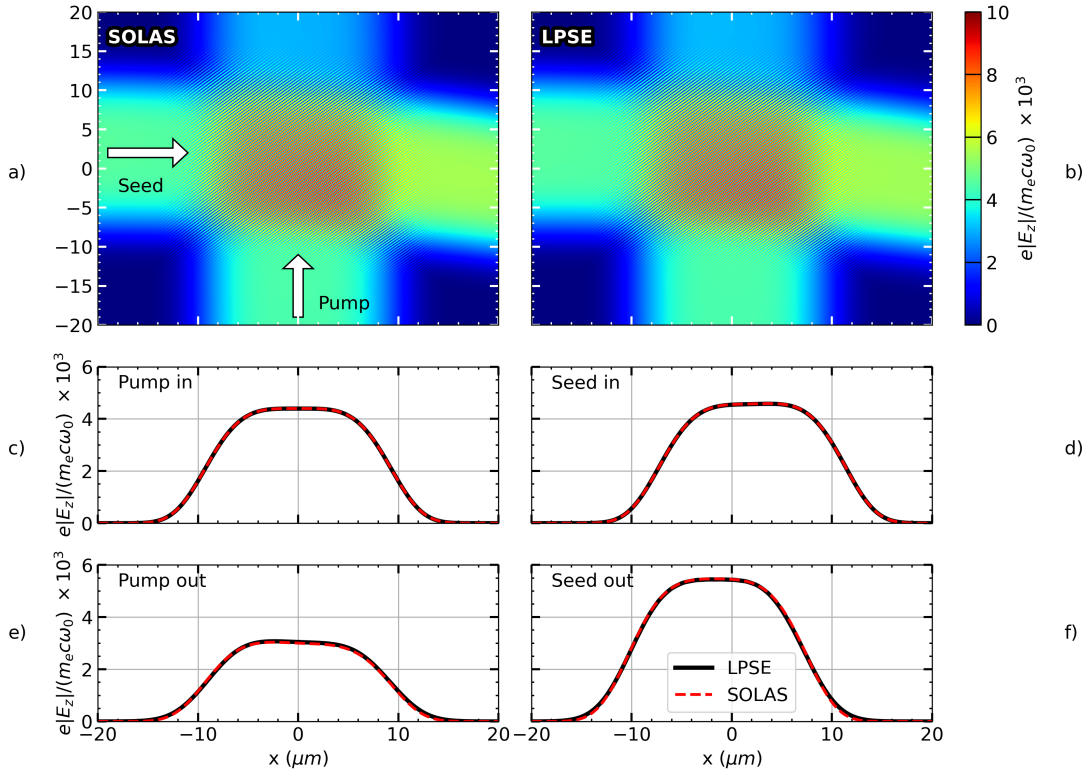


Figure 1.18: This figure shows the results of the 2-D CBET test in the absence of laser caustics. Panels a) & b) show the electric field from the SOLAS & LPSE simulations respectively, after the pump depletion iterations have occurred. Panels c) & e) plot lineouts from the inbound fields of the pump and seed beams respectively for both SOLAS and LPSE. c) & d) plots the same for the outbound fields.

The first test problem is for the case of 2 beams crossing in a non-uniform, non-stationary plasma in the absence of laser caustics. The grid used for the problem was  $x, y \in [-21, 22] \mu\text{m}$  and 2160 cells were used in each direction. This led to a resolution of  $\Delta x \sim \lambda_0/20$  such that the beat field between the 2 beams could be resolved. The electron temperature was uniform,  $T_e = 1 \text{ keV}$ . The density and fluid velocity profiles were,

$$n_e(y) = n_{\text{cr}}(0.006y_{\mu\text{m}} + 0.25), \quad (1.40)$$

$$\mathbf{u}(y) = -\hat{\mathbf{y}}(1.4 - 0.008y_{\mu\text{m}})c_s, \quad (1.41)$$

where  $y_{\mu\text{m}}$  is the coordinate in micro-meters. The beams both had widths  $\sigma = 8.41 \mu\text{m}$  and peak intensities  $I_0 = 2 \times 10^{18} \text{ W/m}^2$ . The beams were defined as *pump* and *seed* and launched from  $\mathbf{x} = [-21, 2] \mu\text{m}$  and  $\mathbf{x} = [0, -21] \mu\text{m}$  along the  $+\hat{\mathbf{x}}$  and  $+ \hat{\mathbf{y}}$  directions respectively. The beam and plasma configuration were chosen to create a strong CBET resonance where the beams cross one another.

Fig. 1.18.a & Fig. 1.18.b show the electric field obtained from the SOLAS & LPSE simulations respectively. It can be seen that the density gradient in  $y$  causes the seed beam to refract somewhat and that CBET results in a significant energy transfer from the pump to the seed

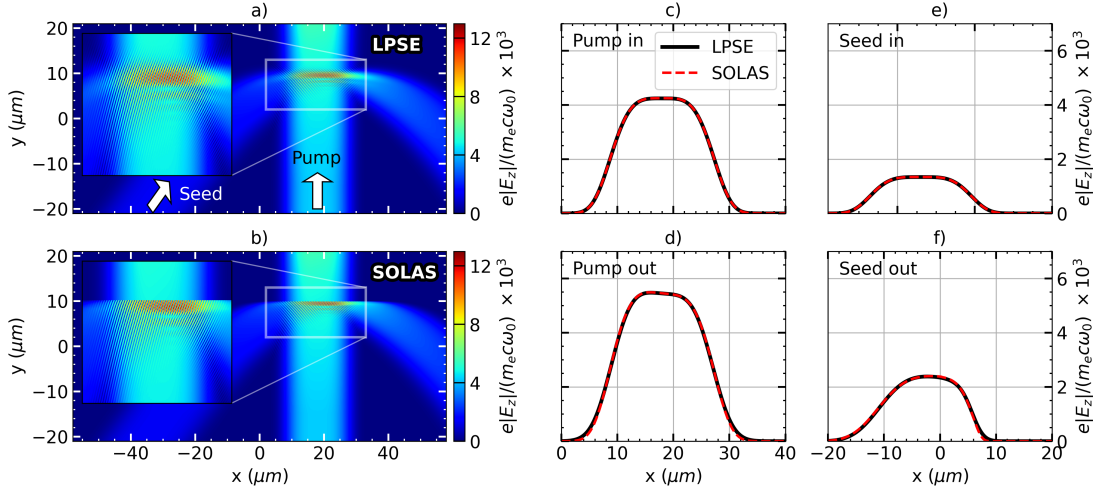


Figure 1.19: This figure shows the results of the 2-D CBET test in the presence of a laser caustic. Panels a) & b) show the electric field from the LPSE & SOLAS simulations respectively. Also plotted is an inset zoom on the caustic region of the seed beam, which demonstrates that SOLAS does not capture the evanescent field. Panels c) & e) plot lineouts from the inbound fields of the pump and seed beams respectively for both SOLAS and LPSE. c) & d) plots the same for the outbound fields.

beam. The lineouts in Fig. 1.18.c, Fig. 1.18.d, Fig. 1.18.e and Fig. 1.18.f all show excellent agreement between SOLAS and Lpse. This is further demonstrated in Tab. 1.2, which lists the ratio of the outgoing seed beam power to the incident power for LPSE, SOLAS and the BEAMCROSSER postprocessor, the results from which are also presented in Ref. [29]. The energy conservation error after the pump depletion iterations was very small,  $\Delta E \sim 10^{-6}$ , as expected because the CBET interaction does not involve any caustics.

### 1.5.7.2 2-D CBET With Caustics

Another 2 beam problem was implemented to test CBET in the presence of a caustic. For this simulation, the grid was  $xy \in [-21, 21] \mu\text{m}$  and  $xy \in [-60, 60] \mu\text{m}$  with a minimum resolution of  $\Delta x = \Delta y \sim \lambda_0/20$ . A uniform electron temperature was used,  $T_e = 2 \text{ keV}$ . The pump beam travels straight up a linear density gradient and therefore does not refract, whereas the seed beam reflects in the gradient and travels out. The beam geometry is chosen so that the pump beam crosses through the middle of the seed beam caustic and the density and flow profiles are tuned to create a resonance at this crossing location,

$$n_e(y) = \begin{cases} 0.02y_{\mu\text{m}} + 0.3, & x \geq -15 \mu\text{m}, \\ 0, & x < -15 \mu\text{m}, \end{cases} \quad (1.42)$$

$$\mathbf{u} = -1.14c_s \hat{\mathbf{y}}. \quad (1.43)$$

Both beams again had widths  $\sigma = 8.41 \mu\text{m}$ . The pump & seed beams were launched from  $\mathbf{x} = [18, -21] \mu\text{m}$  &  $\mathbf{x} = [-35, -21] \mu\text{m}$  pointed along  $\hat{\mathbf{k}} = [0, 1]$  &  $\hat{\mathbf{k}} = [0.707, 0.707]$  respectively. The peak intensities were  $I_0 = 2 \times 10^{18} \text{ W/m}^2$  &  $I_0 = 2 \times 10^{17} \text{ W/m}^2$  for the pump & seed

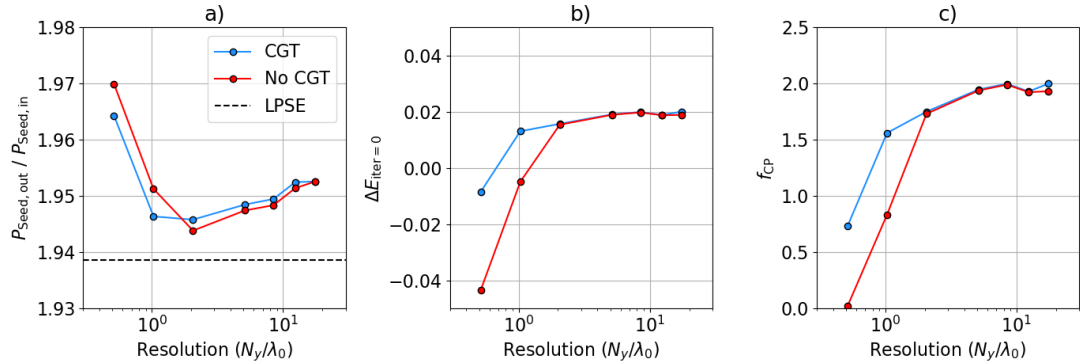


Figure 1.20: This figure shows results from a resolution scan of the 2 beam caustic CBET test both with CGT and without. Plotted in a), b) & c) are the power amplification of the seed beam, initial energy conservation error before energy conservation iterations & caustic pump multiplier used to obtain energy conservation respectively.

respectively.

Fig. 1.19.a and Fig. 1.19.b plot the LPSE and SOLAS<sup>15</sup> total fields respectively. The inset zooms demonstrate that the evanescent fields are not captured in the GO framework. Fig. 1.19.c, Fig. 1.19.d, Fig. 1.19.e & Fig. 1.19.f plot the lineouts of the LPSE and SOLAS field solutions at their exit from the grid, which all demonstrate excellent agreement. The LPSE seed beam amplification was  $P_{\text{seed,out}}/P_{\text{seed,in}} = 1.94$  [29]. This test was run both with and without the CGT model described in Sec. 1.5.2 and at a variety resolutions, to demonstrate how energy conservation at caustics are partially a resolution problem and how CGT mitigates for this somewhat.

Fig. 1.20 plots the results of the resolution scans both with and without CGT. The seed beam amplification after energy conservation iterations is plotted in Fig. 1.20.a, which demonstrates that even at lower resolutions, SOLAS is manages to reproduce the LPSE result to an accuracy of  $\sim \mathcal{O}(1\%)$ . The energy conservation error from the first energy conservation iteration (*i.e.* after the first set of pump depletion iterations, but before energy conservation was achieved), is plotted in Fig. 1.20.b. This plot shows shows convergence in the physics at higher resolutions, although the converged solution (without enforced energy conservation) indicates small errors in the handling of the caustics, which energy conservation is able to correct in an *ad-hoc* manner. Fig. 1.20.c plots the caustic pump multiplier that was required to achieve energy conservation. Both Fig. 1.20.b and Fig. 1.20.c show that CGT improves the convergence of the SOLAS solution when the caustic region width  $\sim \lambda_0$  is not properly resolved by the mesh.

### 1.5.7.3 16 Beam CBET in 2-D

The final CBET test problem presented as validation is a planar, azimuthally symmetric CBET test with 16 beams in a direct-drive like plasma at the OMEGA scale [29]. This problem in-

<sup>15</sup>The field from SOLAS simulation with the minimum resolution,  $\Delta x \sim \lambda_0/20$  is plotted in Fig. 1.19.b.

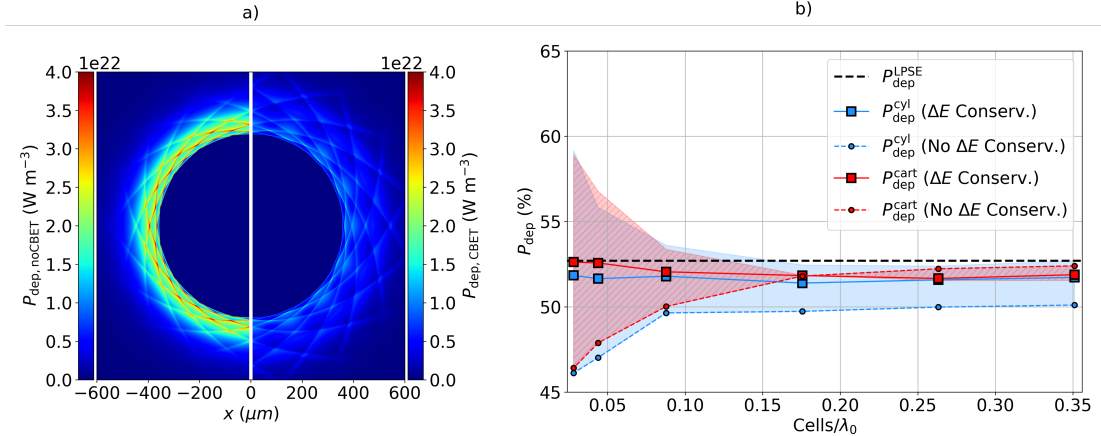


Figure 1.21: Plotted in this figure is the results from the 16 beam CBET test problem. Panel a) plots the deposited power both without (left) and with (right) CBET in cylindrical coordinates at  $1 \mu\text{m}$  radial resolution. Panel b) plots the results of the resolution scan for both Cartesian and cylindrical coordinates. The circles and squares are the values of power deposition without and with enforced energy conservation respectively. The shaded regions illustrate the magnitude of energy conservation error from the initial energy conservation iteration, which can be thought of as the (single-sided) error on the circular points.

volves many beams, all of which undergo laser caustics and CBET scattering with multiple other laser sheets. It is also well suited to test the implementation of the SOLAS CBET model in non-Cartesian geometries, unlike the previous problems which did not have an angle of symmetry. The same setup can be easily initialised in both Cartesian and cylindrical geometry to cross-compare the results.

All beam were pointed toward the origin with an initial starting radius of 1 mm, equally spaced around the circle with a width  $\sigma = 386.8 \mu\text{m}$ . The peak intensity of each beam was  $I_0 = 0.68 \times 10^{18} \text{ W m}^{-2}$  and each had an incident power  $P_{\text{inc}} = 76.3 \text{ TW}$ . The electron temperature was set to  $T_e = 2 \text{ keV}$  and the ion temperature  $T_i = T_e/2$ . The electron density used the profile from Eq. 1.21, with the scale factor,  $S = 1$ . A radial velocity profile was used, which was obtained from a fit to a 1-D LILAC simulation,

$$\mathbf{u}(r) = c_s \left[ M_0 + M_1 \log \left( \frac{r - x_0}{x_1} \right) \right], \quad (1.44)$$

where  $M_0 = 1.41$ ,  $M_1 = 1.37$ ,  $x_0 = 204 \mu\text{m}$  and  $x_1 = 343 \mu\text{m}$ . The Cartesian simulations had a bounding domain  $x, y \in [-800, 800] \mu\text{m}$ , with a resolution ranging from  $\Delta_{x,y} = 1 \rightarrow 12.5 \mu\text{m}$ . The cylindrical simulations had domain  $r \in [0, 800] \mu\text{m}$  and  $\phi \in [-\pi, \pi]$ , with radial resolutions  $\Delta_r = 1 \rightarrow 12.5 \mu\text{m}$  and a fixed  $\phi$  resolution of  $\Delta_\phi = 0.025$ . These simulations are compared to a LPSE simulation of the same problem.

In the absence of CBET, LPSE calculated 90.5 % power deposition. All SOLAS simulations agree with this result to within  $\sim \mathcal{O}(0.1 \%)$ . Including CBET, LPSE obtained an absorption of 52.7 %. Deposited power from the  $\Delta_r = 1 \mu\text{m}$  simulation is plotted in Fig. 1.21.a, both without CBET, and with CBET after energy conservation was achieved. Power deposition

from the Cartesian simulation at  $\Delta_x = 1 \mu\text{m}$  is not plotted, but looks very similar, apart from the small grid artefacts. The reduction in magnitude of deposition is clearly visible, along with a slight radial broadening of the deposition region. The angled-line features in both plots are from the casutic region of the beam, where a 16-fold symmetry can be seen in both of the results, due to the beam geometry of the problem. The finer scale thin structures in both of these plots is due to enhanced deposition occurring at the beam casutic, where the ray amplitude swells to a maximum, enhancing the field strength.

Plotted in Fig. 1.21.b are the values of deposited power in the presence of CBET for both the cylindrical and Cartesian simulations, compared to the LPSE result. Circular markers are the values obtained for CBET deposition after the first set of pump-depletion iterations, *i.e.* before energy conservation was achieved. The larger square markers are the results after energy conservation was achieved. Shaded regions correspond to the magnitude and sign of the energy conservation error,  $\Delta E_{j=0}$ , *before* energy conservation was achieved, *i.e.*, for the circular points. This region corresponds to the deposition that could be achieved if any, arbitrary approach was taken to enforce conservation, for example if the value  $\Delta E_{j=0} = \pm 10\%$  for one simulation, then up to 10 % could be added to (subtracted from)  $P_{\text{dep}}$ . The trend, especially at lower resolution demonstrates that enforcing energy conservation brings the SOLAS result closer to LPSE, motivating the use of the approach in later chapters of this thesis. Although the cylindrical results typically appear to have a larger value for  $\Delta E_{j=0}$  compared to the Cartesian results, the post conservation results are all deemed sufficiently close to both the Cartesian result and LPSE. The saturation of error for cylindrical geometry at higher radial resolutions seem to indicate that  $\Delta E_{j=0}$  is dominated by the  $\phi$  resolution in this region, which was kept fixed across all simulations.

## 1.6 Simulations of CBET for OMEGA Direct-Drive Implosions

This Section shall present CHIMERA-SOLAS simulations of OMEGA direct-drive implosions. In Sec. 1.6.1, 1-D Rad-Hydro simulations of OMEGA shot 89224 coupled to a 3-D raytrace from SOLAS will be presented, both with and without the effect of CBET. This illustrates that the implementation of the CBET model in SOLAS correctly captures the loss of drive efficiency. In Sec. 1.6.1, 3-D SOLAS post-processes of, spherically symmetric hydrodynamic data from the LILAC code shall be presented both with and without CBET, alongside comparisons to the 3-D CBET codes IFRIIT and BEAMCROSSER. These simulations demonstrate that the SOLAS CBET model also correctly captures the enhancement of beam-mode drive asymmetry introduced by CBET in spherical illumination geometries.

### 1.6.1 1-D hydrodynamics, 3-D Ray-Trace Simulation of OMEGA Shot 89224

A 1-D CHIMERA-SOLAS Rad-Hydro simulation of OMEGA 89224 was performed to illustrate the effect that CBET has on drive efficiency of direct-drive implosions. Drive efficiency is lost primarily due a reduction in the magnitude of deposited energy. A secondary effect is that the radii where deposition occurs is pushed slightly further away from the ablation surface.

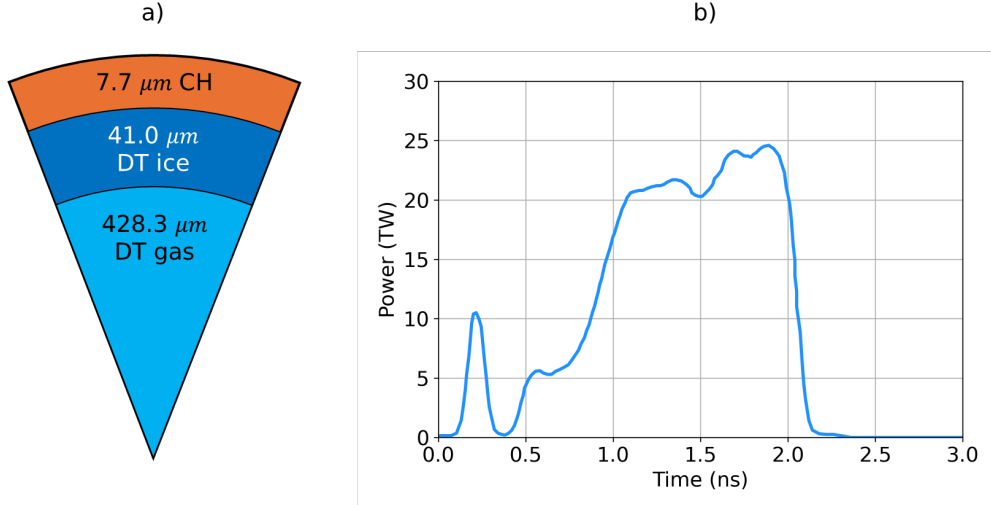


Figure 1.22: This figure shows the initial conditions for OMEGA shot 89224. The shot was a cryogenic, DT implosion with materials and radii shown in panel a). Panel b) plots the incident laser pulse shape.

Table 1.2: Integrated metrics from simulations of OMEGA 89224. LILAC metrics are from Refs. [70–72].

	Yield ( $\times 10^{14}$ )	$\langle T_i \rangle$ (keV)	$t_{\text{bang}}$ (ns)	$V_{\text{imp}}$ (km/s)
LILAC, CBET	4.00	4.8	2.17	476
CHIMERA, CBET	1.78	4.2	2.16	490
CHIMERA, no CBET	6.77	6.2	1.94	661

This happens because beams only lose energy inside of the CBET resonance volume, which for backscatter CBET occurs at the Mach-1 surface, as explained in Sec. ???. Therefore the deposited power vs. radius curve is shifted to slightly higher radii. Both of these effects by a 3-D CBET model coupled to 1-D Rad-Hydro.

The initial conditions for shot 89224 are plotted in Fig. 1.22.a, with vacuum outside the outer radius. A tabulated Sesame table of state was used for each material [73] and a  $P_{1/3}$  radiation transport algorithm was used with tabulated opacities and emissivities from the SPK code [74]. Thermal conduction was solved with a fully implicit scheme. The electron flux limiter was set by using the default CHIMERA direct-drive method,

$$f_{\text{lim},e} = \begin{cases} 0.06, & \text{if in picket pulse} \\ 0.15, & \text{otherwise.} \end{cases} \quad (1.45)$$

The simulation domain was  $r \in [0, 1680]$   $\mu\text{m}$ , with a fixed radial resolution  $\Delta_r = 1$   $\mu\text{m}$ . Two simulations were conducted, one with the effect of CBET on power deposition and one without. In order to load balance the ray trace and discretise CBET interactions between different beams around the spherical  $4\pi$  sr, SOLAS used a sparse angular grid with  $N_\phi = 51$  &  $N_\theta = 30$  azimuthal and polar cells respectively. At times earlier than 10 ps, a *cold start* routine was

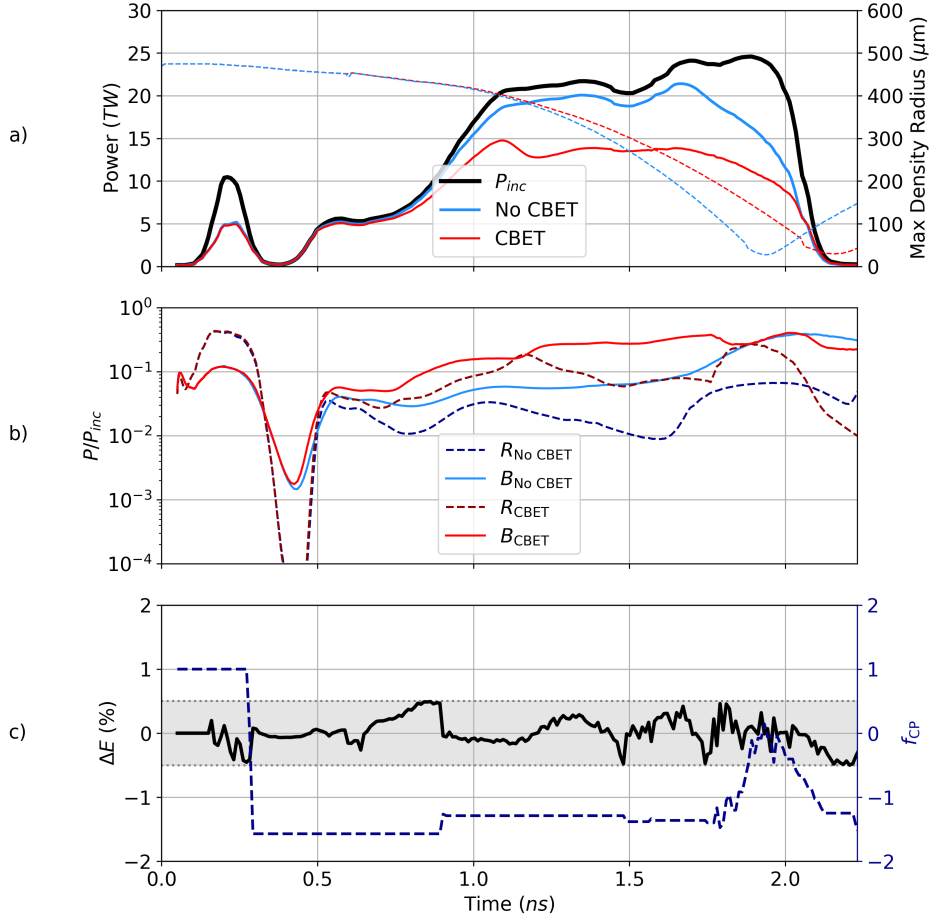


Figure 1.23: This figure shows the results of a CHIMERA-SOLAS simulation of OMEGA shot 89224. Panel a) shows the deposited power both from 2 separate simulations of 89224, one with & one without CBET as red & blue solid curves respectively. The shell radius, defined at the radius of maximum density, is also plotted on the right axis as dashed curves. Panel b) plots the time resolved partition of non-absorbed light for these simulations. Plotted in c) is the energy conservation error after energy conservation was achieved, alongside the value of  $f_{CP}$  that was used to achieve conservation.

employed, where 50 % of the incident power was deposited at the critical radius to create a finite scale length of underdense plasma, which rays could deposit and refract in. Raytraces were conducted every hydrodynamic timestep, without computing CBET up to 150 ps<sup>16</sup> after which a full raytrace routine, including the effect of CBET was conducted every 10 ps. For hydrodynamic steps in between these CBET raytraces, the most recently computed  $P_{dep}$  profile (normalised to 1 and then scaled to the incident power), was used as the laser source term for the timestep. Parameter scans of the raytrace frequency confirmed that the behaviour of OMEGA simulations is well converged with this frequency.

The spatially integrated absorbed power is plotted in Fig. 1.23.a as solid curves.

<sup>16</sup>Note that the very low intensity from this section of the pulse means that the CBET gains are negligible.

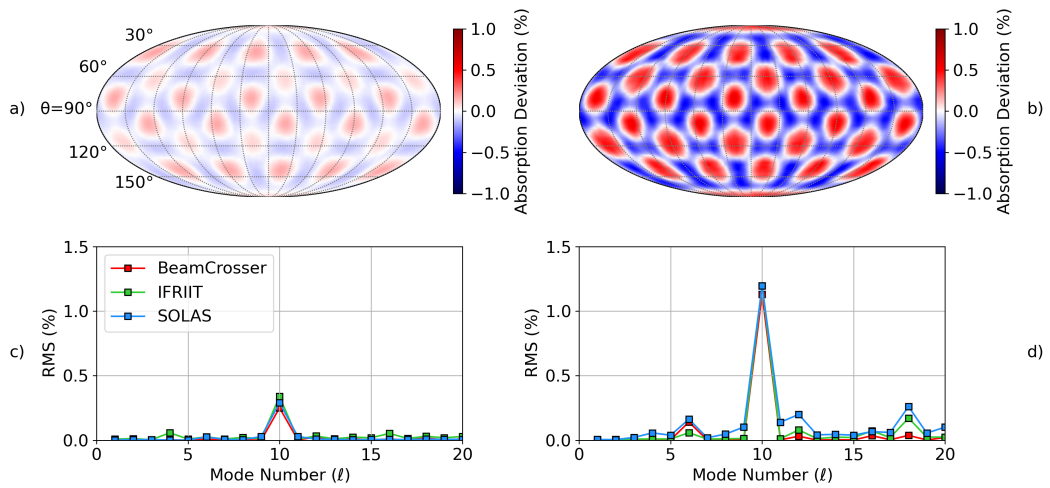


Figure 1.24: This figure shows the results from a 3-D SOLAS post-process of spherically symmetric hydrodynamic data obtained from a LILAC simulation of an OMEGA direct-drive implosion. Figures a) and b) show the deviation in radially integrated deposited power without and with CBET respectively. Figures c) and d) plot the spherical harmonic modal decomposition for these maps alongside results from the IFRIIT and BEAMCROSSER codes without and with CBET respectively.

Show the absorbed power vs time and effect of CBET. Show instantaneous radial profiles. Show integrated parameter comparison to LILAC post-shot simulation. Describe the previous method of tuning, involving a 2D scan of flux limiter and power multipliers. Say how it's great that the  $f_{lime} = 0.06 \rightarrow 0.15$  and CBET combination now gives a predictive capability for OMEGA shots.

## 1.6.2 3-D Post Process of Absorption Non-Uniformity

Mention how the model can also be used as a postprocess. CHIMERA can restart from 1-D data into spherically symmetric 3-D profiles. Ray Trace and CBET can then be performed through these profiles to understand the absorption non-uniformity present due to CBET. Note that comparison of 1-D and 3-D simulations shows that thermal conduction does a good job of smoothing angular deviations in coronal plasma conditions. The assumption of spherically symmetric profiles for the laser is therefore deemed valid, and it is a technique typically used by post-process CBET codes.

MAYBE?? Mention how ray noise means that we can't use direct deposition. Therefore use Pdep from field estimate, which is much cleaner.

Talk about how CBET enhances angular non-uniformity. Show modal decomposition.

## 1.7 Future Model Extensions

Say that there is even more laser/ CBET physics that is interesting and can be implemented within the ray-tracing framework. Some are straightforward to implement, while others more difficult and computationally expensive.

### 1.7.1 Langdon Effect on Absorption

Describe Langdon from a kinetic perspective and why it reduces absorption. Describe how you can fit it and include as a modification to ray-tracing absorption if you have the field/intensity. Describe the magnitude of the effect for ICF like conditions. Describe briefly how it would be implemented, say it would not be difficult.

### 1.7.2 Langdon Effect on CBET

Describe what this is. Say that it is important for high overlapping intensities, eg hohlraum LEH. Say that it is thought to stabilise the CBET interaction in indirect drive configurations and remove the need for artificial clamps. Describe briefly how it would be implemented, say it would not be difficult.

### 1.7.3 Polarised CBET

Describe how ion acoustic waves are driven by beat between electric fields from light and therefore is polarisation dependent. Say how on OMEGA, RPP smoothing means that each beam is split into 2 sub-beams with linear polarisation. Say that these do not have a symmetry to the configuration about the sphere. Say that this leads to mode-1 on OMEGA. Say that you can track polarisation of rays and trace these sub-beams independently. Would make it more expensive, but definitely feasible.

### 1.7.4 Bandwidth for CBET Mitigation Studies

Describe how bandwidth should reduce LPI growth rates. Understanding the desired bandwidth to mitigate CBET is a key consideration for design of future laser systems. Fields can be modified to include discrete wavelengths to model bandwidth.

### 1.7.5 Additional LPIs

Could look at TPD, SBS and SRS. In theory not a difficult problem to do backscatter, but side-SRS is difficult, because additional rays would need to be launched. This could make the model more useful to indirect-drive experiments and design of ignition scale direct-drive facilities, where SRS is thought to be important energetically due to long scale lengths.

---

## 1.8 Conclusions

Say that the chapter has described the validity and implementation of SOLAS and validated it. Culminated in demonstrating that the model can reproduce post-shot simulations of an OMEGA shot from the LILAC code which includes a CBET model. This demonstrates that the CHIMERA code now has a predictive capability for OMEGA scale direct drive experiments, as no free parameter tuning was required.

# **Appendices**

## A Numerics Appendices



# Bibliography

- [1] P. Tzeferacos, A. Rigby, A. F. A. Bott, A. R. Bell, R. Bingham, A. Casner, F. Cattaneo, E. M. Churazov, J. Emig, F. Fiuzza, C. B. Forest, J. Foster, C. Graziani, J. Katz, M. Koenig, C.-K. Li, J. Meinecke, R. Petrasso, H.-S. Park, B. A. Remington, J. S. Ross, D. Ryu, D. Ryutov, T. G. White, B. Reville, F. Miniati, A. A. Schekochihin, D. Q. Lamb, D. H. Froula, and G. Gregori. Laboratory evidence of dynamo amplification of magnetic fields in a turbulent plasma. *Nature Communications*, 9(1):591, February 2018. ISSN 2041-1723. doi: 10.1038/s41467-018-02953-2. URL <https://www.nature.com/articles/s41467-018-02953-2>. 6
- [2] F. Fiuzza, G. F. Swadling, A. Grassi, H. G. Rinderknecht, D. P. Higginson, D. D. Ryutov, C. Bruulsema, R. P. Drake, S. Funk, S. Glenzer, G. Gregori, C. K. Li, B. B. Pollock, B. A. Remington, J. S. Ross, W. Rozmus, Y. Sakawa, A. Spitkovsky, S. Wilks, and H.-S. Park. Electron acceleration in laboratory-produced turbulent collisionless shocks. *Nature Physics*, 16(9):916–920, September 2020. ISSN 1745-2481. doi: 10.1038/s41567-020-0919-4. URL <https://www.nature.com/articles/s41567-020-0919-4>. Publisher: Nature Publishing Group.
- [3] Jena Meinecke, Petros Tzeferacos, James S. Ross, Archie F. A. Bott, Scott Feister, Hye-Sook Park, Anthony R. Bell, Roger Blandford, Richard L. Berger, Robert Bingham, Alexis Casner, Laura E. Chen, John Foster, Dustin H. Froula, Clement Goyon, Daniel Kalantar, Michel Koenig, Brandon Lahmann, Chikang Li, Yingchao Lu, Charlotte A. J. Palmer, Richard D. Petrasso, Hannah Poole, Bruce Remington, Brian Reville, Adam Reyes, Alexandra Rigby, Dongsu Ryu, George Swadling, Alex Zylstra, Francesco Miniati, Subir Sarkar, Alexander A. Schekochihin, Donald Q. Lamb, and Gianluca Gregori. Strong suppression of heat conduction in a laboratory replica of galaxy-cluster turbulent plasmas. *Science Advances*, 8(10):eabj6799, March 2022. ISSN 2375-2548. doi: 10.1126/sciadv.abj6799. URL <https://www.science.org/doi/10.1126/sciadv.abj6799>. 6
- [4] Andrea L. Kritcher, Damian C. Swift, Tilo Döppner, Benjamin Bachmann, Lorin X. Benedict, Gilbert W. Collins, Jonathan L. DuBois, Fred Elsner, Gilles Fontaine, Jim A. Gaffney, Sébastien Hamel, Amy Lazicki, Walter R. Johnson, Natalie Kostinski, Dominik Kraus, Michael J. MacDonald, Brian Maddox, Madison E. Martin, Paul Neu-mayer, Abbas Nikroo, Joseph Nilsen, Bruce A. Remington, Didier Saumon, Phillip A. Sterne, Wendi Sweet, Alfredo A. Correa, Heather D. Whitley, Roger W. Falcone, and Siegfried H. Glenzer. A measurement of the equation of state of carbon envelopes of white dwarfs. *Nature*, 584(7819):51–54, August 2020. ISSN 0028-0836, 1476-

4687. doi: 10.1038/s41586-020-2535-y. URL <https://www.nature.com/articles/s41586-020-2535-y>. 6
- [5] R. F. Smith, J. H. Eggert, R. Jeanloz, T. S. Duffy, D. G. Braun, J. R. Patterson, R. E. Rudd, J. Biener, A. E. Lazicki, A. V. Hamza, J. Wang, T. Braun, L. X. Benedict, P. M. Celliers, and G. W. Collins. Ramp compression of diamond to five terapascals. *Nature*, 511(7509): 330–333, July 2014. ISSN 1476-4687. doi: 10.1038/nature13526. URL <https://www.nature.com/articles/nature13526>. Publisher: Nature Publishing Group. 6
- [6] A. B. Zylstra, O. A. Hurricane, D. A. Callahan, A. L. Kritcher, J. E. Ralph, H. F. Robey, J. S. Ross, C. V. Young, K. L. Baker, D. T. Casey, T. Döppner, L. Divol, M. Hohenberger, S. Le Pape, A. Pak, P. K. Patel, R. Tommasini, S. J. Ali, P. A. Amendt, L. J. Atherton, B. Bachmann, D. Bailey, L. R. Benedetti, L. Berzak Hopkins, R. Betti, S. D. Bhandarkar, J. Biener, R. M. Bionta, N. W. Birge, E. J. Bond, D. K. Bradley, T. Braun, T. M. Briggs, M. W. Bruhn, P. M. Celliers, B. Chang, T. Chapman, H. Chen, C. Choate, A. R. Christopherson, D. S. Clark, J. W. Crippen, E. L. Dewald, T. R. Dittrich, M. J. Edwards, W. A. Farmer, J. E. Field, D. Fittinghoff, J. Frenje, J. Gaffney, M. Gatu Johnson, S. H. Glenzer, G. P. Grim, S. Haan, K. D. Hahn, G. N. Hall, B. A. Hammel, J. Harte, E. Hartouni, J. E. Heebner, V. J. Hernandez, H. Herrmann, M. C. Herrmann, D. E. Hinkel, D. D. Ho, J. P. Holder, W. W. Hsing, H. Huang, K. D. Humbird, N. Izumi, L. C. Jarrott, J. Jeet, O. Jones, G. D. Kerbel, S. M. Kerr, S. F. Khan, J. Kilkenny, Y. Kim, H. Geppert Kleinrath, V. Geppert Kleinrath, C. Kong, J. M. Koning, J. J. Kroll, M. K. G. Kruse, B. Kustowski, O. L. Landen, S. Langer, D. Larson, N. C. Lemos, J. D. Lindl, T. Ma, M. J. MacDonald, B. J. MacGowan, A. J. Mackinnon, S. A. MacLaren, A. G. MacPhee, M. M. Marinak, D. A. Mariscal, E. V. Marley, L. Masse, K. Meaney, N. B. Meezan, P. A. Michel, M. Millot, J. L. Milovich, J. D. Moody, A. S. Moore, J. W. Morton, T. Murphy, K. Newman, J.-M. G. Di Nicola, A. Nikroo, R. Nora, M. V. Patel, L. J. Pelz, J. L. Peterson, Y. Ping, B. B. Pollock, M. Ratledge, N. G. Rice, H. Rinderknecht, M. Rosen, M. S. Rubery, J. D. Salmonson, J. Sater, S. Schiaffino, D. J. Schlossberg, M. B. Schneider, C. R. Schroeder, H. A. Scott, S. M. Sepke, K. Sequoia, M. W. Sherlock, S. Shin, V. A. Smalyuk, B. K. Spears, P. T. Springer, M. Stadermann, S. Stoupin, D. J. Strozzi, L. J. Suter, C. A. Thomas, R. P. J. Town, E. R. Tubman, C. Trosseille, P. L. Volegov, C. R. Weber, K. Widmann, C. Wild, C. H. Wilde, B. M. Van Wonterghem, D. T. Woods, B. N. Woodworth, M. Yamaguchi, S. T. Yang, and G. B. Zimmerman. Burning plasma achieved in inertial fusion. *Nature*, 601(7894):542–548, January 2022. ISSN 1476-4687. doi: 10.1038/s41586-021-04281-w. URL <https://www.nature.com/articles/s41586-021-04281-w>. Publisher: Nature Publishing Group. 6
- [7] Stephen A. Slutz and Roger A. Vesey. High-Gain Magnetized Inertial Fusion. *Physical Review Letters*, 108(2):025003, January 2012. ISSN 0031-9007, 1079-7114. doi: 10.1103/PhysRevLett.108.025003. URL <https://link.aps.org/doi/10.1103/PhysRevLett.108.025003>.
- [8] C. A. Williams, R. Betti, V. Gopalaswamy, J. P. Knauer, C. J. Forrest, A. Lees, R. Ejaz,

- P. S. Farmakis, D. Cao, P. B. Radha, K. S. Anderson, S. P. Regan, V. Yu Glebov, R. C. Shah, C. Stoeckl, S. Ivancic, K. Churnetski, R. T. Janezic, C. Fella, M. J. Rosenberg, M. J. Bonino, D. R. Harding, W. T. Shmayda, J. Carroll-Nellenback, S. X. Hu, R. Epstein, T. J. B. Collins, C. A. Thomas, I. V. Igumenshchev, V. N. Goncharov, W. Theobald, K. M. Woo, J. A. Marozas, K. A. Bauer, S. Sampat, L. J. Waxer, D. Turnbull, P. V. Heuer, H. McClow, L. Ceuvorst, W. Scullin, D. H. Edgell, M. Koch, D. Bredesen, M. Gatu Johnson, J. A. Frenje, R. D. Petrasso, C. Shuldborg, M. Farrell, J. Murray, D. Guzman, B. Serrato, S. F. B. Morse, M. Labuzeta, C. Deeney, and E. M. Campbell. Demonstration of hot-spot fuel gain exceeding unity in direct-drive inertial confinement fusion implosions. *Nature Physics*, 20(5):758–764, May 2024. ISSN 1745-2481. doi: 10.1038/s41567-023-02363-2. URL <https://www.nature.com/articles/s41567-023-02363-2>. Publisher: Nature Publishing Group.
- [9] K. L. Nguyen, L. Yin, B. J. Albright, A. M. Hansen, D. H. Froula, D. Turnbull, R. K. Follett, and J. P. Palastro. Cross-beam energy transfer saturation by ion trapping-induced detuning. *Physics of Plasmas*, 28(8):082705, August 2021. ISSN 1070-664X, 1089-7674. doi: 10.1063/5.0054008. URL <https://pubs.aip.org/aip/pop/article/106807>. 6, 10
- [10] J. F. Myatt, R. K. Follett, J. G. Shaw, D. H. Edgell, D. H. Froula, I. V. Igumenshchev, and V. N. Goncharov. A wave-based model for cross-beam energy transfer in direct-drive inertial confinement fusion. *Physics of Plasmas*, 24(5):056308, April 2017. ISSN 1070-664X. doi: 10.1063/1.4982059. URL <https://doi.org/10.1063/1.4982059>. 6, 10, 34
- [11] Andrew J. Schmitt and Stephen P. Obenschain. The importance of laser wavelength for driving inertial confinement fusion targets. II. Target design. *Physics of Plasmas*, 30(1):012702, January 2023. ISSN 1070-664X. doi: 10.1063/5.0118093. URL <https://doi.org/10.1063/5.0118093>. 7
- [12] Andrew J. Schmitt and Stephen P. Obenschain. The importance of laser wavelength for driving inertial confinement fusion targets. I. Basic physics. *Physics of Plasmas*, 30(1):012701, January 2023. ISSN 1070-664X, 1089-7674. doi: 10.1063/5.0118080. URL <https://pubs.aip.org/pop/article/30/1/012701/2867678/The-importance-of-laser-wavelength-for-driving>. 7
- [13] J Huba, D. NRL Plasma Formulary. Technical Report NRL/PU/6790-13-589, Naval Research Laboratory, Washington, DC, 2013. 7
- [14] Tudor Wyatt Johnston and John M. Dawson. Correct values for high-frequency power absorption by inverse bremsstrahlung in plasmas. *Physics of Fluids*, 16:722–722, May 1973. ISSN 0899-82131070-6631. doi: 10.1063/1.1694419. URL <https://ui.adsabs.harvard.edu/abs/1973PhFl...16..722J>. Publisher: AIP ADS Bibcode: 1973PhFl...16..722J. 7

- [15] A. Colaïtis, I. Igumenshchev, J. Mathiaud, and V. Goncharov. Inverse ray tracing on icosahedral tetrahedron grids for non-linear laser plasma interaction coupled to 3D radiation hydrodynamics. *Journal of Computational Physics*, 443:110537, October 2021. ISSN 0021-9991. doi: 10.1016/j.jcp.2021.110537. URL <https://www.sciencedirect.com/science/article/pii/S0021999121004320>. 7, 8, 17, 18, 28
- [16] C. J. Randall, James R. Albritton, and J. J. Thomson. Theory and simulation of stimulated Brillouin scatter excited by nonabsorbed light in laser fusion systems. *The Physics of Fluids*, 24(8):1474–1484, August 1981. ISSN 0031-9171. doi: 10.1063/1.863551. URL <https://doi.org/10.1063/1.863551>. 7, 34, 36
- [17] A. Colaïtis, G. Duchateau, P. Nicolaï, and V. Tikhonchuk. Towards modeling of nonlinear laser-plasma interactions with hydrocodes: The thick-ray approach. *Physical Review E*, 89(3):033101, March 2014. doi: 10.1103/PhysRevE.89.033101. URL <https://link.aps.org/doi/10.1103/PhysRevE.89.033101>. Publisher: American Physical Society. 7, 9
- [18] R. W. Paddock, H. Martin, R. T. Ruskov, R. H. H. Scott, W. Garbett, B. M. Haines, A. B. Zylstra, R. Aboushelbaya, M. W. Mayr, B. T. Spiers, R. H. W. Wang, and P. A. Norreys. One-dimensional hydrodynamic simulations of low convergence ratio direct-drive inertial confinement fusion implosions. *Philosophical Transactions of the Royal Society A: Mathematical, Physical and Engineering Sciences*, 379(2189):20200224, January 2021. ISSN 1364-503X, 1471-2962. doi: 10.1098/rsta.2020.0224. URL <https://royalsocietypublishing.org/doi/10.1098/rsta.2020.0224>. 7
- [19] A. Colaïtis, J. P. Palastro, R. K. Follett, I. V. Igumenschev, and V. Goncharov. Real and complex valued geometrical optics inverse ray-tracing for inline field calculations. *Physics of Plasmas*, 26(3):032301, March 2019. ISSN 1070-664X, 1089-7674. doi: 10.1063/1.5082951. URL <https://pubs.aip.org/pop/article/26/3/032301/699557/Real-and-complex-valued-geometrical-optics-inverse>. 8, 29, 30, 32
- [20] A. Colaïtis, R. K. Follett, J. P. Palastro, I. Igumenschev, and V. Goncharov. Adaptive inverse ray-tracing for accurate and efficient modeling of cross beam energy transfer in hydrodynamics simulations. *Physics of Plasmas*, 26(7):072706, July 2019. ISSN 1070-664X, 1089-7674. doi: 10.1063/1.5108777. URL <https://pubs.aip.org/pop/article/26/7/072706/1060189/Adaptive-inverse-ray-tracing-for-accurate-and>. 8, 29
- [21] D. J. Strozzi, D. S. Bailey, P. Michel, L. Divol, S. M. Sepke, G. D. Kerbel, C. A. Thomas, J. E. Ralph, J. D. Moody, and M. B. Schneider. Interplay of Laser-Plasma Interactions and Inertial Fusion Hydrodynamics. *Physical Review Letters*, 118(2):025002, January 2017. ISSN 0031-9007, 1079-7114. doi: 10.1103/PhysRevLett.118.025002. URL <https://link.aps.org/doi/10.1103/PhysRevLett.118.025002>. 8
- [22] S. Liberatore, P. Gauthier, J. L. Willien, P. E. Masson-Laborde, F. Philippe, O. Poujade, E. Alozy, R. Botrel, G. Boutoux, J. Bray, T. Caillaud, C. Chicanne, C. Chollet,

- A. Debayle, S. Depierreux, W. Duchastenier, M. Ferri, O. Henry, P. Hoch, S. Laffite, O. Landoas, L. Le-Deroff, E. Lefebvre, G. Legay, I. Marmajou, C. Meyer, K. Molina, O. Morice, E. Peche, P. Prunet, R. Riquier, R. Rosch, V. Tassin, X. Vaisseau, and B. Villette. First indirect drive inertial confinement fusion campaign at Laser Megajoule. *Physics of Plasmas*, 30(12):122707, December 2023. ISSN 1070-664X, 1089-7674. doi: 10.1063/5.0176446. URL <https://pubs.aip.org/pop/article/30/12/122707/2930727/First-indirect-drive-inertial-confinement-fusion>. 8
- [23] J. A. Marozas, M. Hohenberger, M. J. Rosenberg, D. Turnbull, T. J. B. Collins, P. B. Radha, P. W. McKenty, J. D. Zuegel, F. J. Marshall, S. P. Regan, T. C. Sangster, W. Seka, E. M. Campbell, V. N. Goncharov, M. W. Bowers, J.-M. G. Di Nicola, G. Erbert, B. J. MacGowan, L. J. Pelz, J. Moody, and S. T. Yang. Wavelength-detuning cross-beam energy transfer mitigation scheme for direct drive: Modeling and evidence from National Ignition Facility implosions. *Physics of Plasmas*, 25(5):056314, May 2018. ISSN 1070-664X, 1089-7674. doi: 10.1063/1.5022181. URL <https://pubs.aip.org/pop/article/25/5/056314/1061159/Wavelength-detuning-cross-beam-energy-transfer>. 8, 17, 18, 19, 35
- [24] A. Debayle, C. Ruyer, O. Morice, P.-E. Masson-Laborde, P. Loiseau, and D. Benisti. A unified modeling of wave mixing processes with the ray tracing method. *Physics of Plasmas*, 26(9):092705, September 2019. ISSN 1070-664X, 1089-7674. doi: 10.1063/1.5110247. URL <https://pubs.aip.org/pop/article/26/9/092705/263616/A-unified-modeling-of-wave-mixing-processes-with>. 8
- [25] A. Colaïtis, S. Hüller, D. Pesme, G. Duchateau, and V. T. Tikhonchuk. Crossed beam energy transfer: Assessment of the paraxial complex geometrical optics approach versus a time-dependent paraxial method to describe experimental results. *Physics of Plasmas*, 23(3):032118, March 2016. ISSN 1070-664X, 1089-7674. doi: 10.1063/1.4944496. URL <https://pubs.aip.org/pop/article/23/3/032118/1016773/Crossed-beam-energy-transfer-Assessment-of-the>. 9
- [26] A. Colaïtis, G. Duchateau, X. Ribeyre, and V. Tikhonchuk. Modeling of the cross-beam energy transfer with realistic inertial-confinement-fusion beams in a large-scale hydrocode. *Physical Review E*, 91(1):013102, January 2015. ISSN 1539-3755, 1550-2376. doi: 10.1103/PhysRevE.91.013102. URL <https://link.aps.org/doi/10.1103/PhysRevE.91.013102>. 9
- [27] D. H. Edgell, R. K. Follett, I. V. Igumenshchev, J. F. Myatt, J. G. Shaw, and D. H. Froula. Mitigation of cross-beam energy transfer in symmetric implosions on OMEGA using wavelength detuning. *Physics of Plasmas*, 24(6):062706, June 2017. ISSN 1070-664X, 1089-7674. doi: 10.1063/1.4985315. URL <https://pubs.aip.org/aip/pop/article/108749>. 10
- [28] R. K. Follett, J. G. Shaw, J. F. Myatt, V. N. Goncharov, D. H. Edgell, D. H. Froula, and J. P. Palastro. Ray-based modeling of cross-beam energy transfer at caustics. *Physical Review E*, 98(4):043202, October 2018. ISSN 2470-0045, 2470-0053. doi: 10.

- 1103/PhysRevE.98.043202. URL <https://link.aps.org/doi/10.1103/PhysRevE.98.043202>. 10, 29, 38, 39
- [29] R. K. Follett, A. Colaïtis, D. Turnbull, D. H. Froula, and J. P. Palastro. Validation of ray-based cross-beam energy transfer models. *Physics of Plasmas*, 29(11):113902, November 2022. ISSN 1070-664X, 1089-7674. doi: 10.1063/5.0123462. URL <https://pubs.aip.org/pop/article/29/11/113902/2844248/Validation-of-ray-based-cross-beam-energy-transfer>. 10, 25, 28, 29, 30, 33, 37, 44, 45, 47, 48
- [30] Jason F. Myatt, John G. Shaw, Russell K. Follett, Dana H. Edgell, Dustin H. Froula, John P. Palastro, and Valeri N. Goncharov. LPSE: A 3-D wave-based model of cross-beam energy transfer in laser-irradiated plasmas. *Journal of Computational Physics*, 399:108916, December 2019. ISSN 00219991. doi: 10.1016/j.jcp.2019.108916. URL <https://linkinghub.elsevier.com/retrieve/pii/S0021999119306217>. 10
- [31] R. K. Follett, J. G. Shaw, J. F. Myatt, H. Wen, D. H. Froula, and J. P. Palastro. Thresholds of absolute two-plasmon-decay and stimulated Raman scattering instabilities driven by multiple broadband lasers. *Physics of Plasmas*, 28(3):032103, March 2021. ISSN 1070-664X, 1089-7674. doi: 10.1063/5.0037869. URL <https://pubs.aip.org/pop/article/28/3/032103/835482/Thresholds-of-absolute-two-plasmon-decay-and>. 10
- [32] L. J. Perkins, R. Betti, K. N. LaFortune, and W. H. Williams. Shock Ignition: A New Approach to High Gain Inertial Confinement Fusion on the National Ignition Facility. *Physical Review Letters*, 103(4):045004, July 2009. ISSN 0031-9007, 1079-7114. doi: 10.1103/PhysRevLett.103.045004. URL <https://link.aps.org/doi/10.1103/PhysRevLett.103.045004>. 10
- [33] A. G. Seaton, L. Yin, R. K. Follett, B. J. Albright, and A. Le. Cross-beam energy transfer in direct-drive ICF. I. Nonlinear and kinetic effects. *Physics of Plasmas*, 29(4):042706, April 2022. ISSN 1070-664X. doi: 10.1063/5.0078800. URL <https://doi.org/10.1063/5.0078800>. 10
- [34] A. G. Seaton, L. Yin, R. K. Follett, B. J. Albright, and A. Le. Cross-beam energy transfer in direct-drive ICF. II. Theory and simulation of mitigation through increased laser bandwidth. *Physics of Plasmas*, 29(4):042707, April 2022. ISSN 1070-664X. doi: 10.1063/5.0078801. URL <https://doi.org/10.1063/5.0078801>. 10
- [35] J. P. Chittenden, B. D. Appelbe, F. Manke, K. McGlinchey, and N. P. L. Niasse. Signatures of asymmetry in neutron spectra and images predicted by three-dimensional radiation hydrodynamics simulations of indirect drive implosions. *Physics of Plasmas*, 23(5):052708, May 2016. ISSN 1070-664X. doi: 10.1063/1.4949523. URL <https://doi.org/10.1063/1.4949523>. 14

- [36] Hyeong-Bin Cheong and Hyun-Gyu Kang. Eigensolutions of the spherical Laplacian for the cubed-sphere and icosahedral-hexagonal grids. *Quarterly Journal of the Royal Meteorological Society*, 141(693):3383–3398, October 2015. ISSN 0035-9009, 1477-870X. doi: 10.1002/qj.2620. URL <https://rmets.onlinelibrary.wiley.com/doi/10.1002/qj.2620>. 15
- [37] Zinovy Malkin. A New Equal-area Isolatitudinal Grid on a Spherical Surface. *The Astronomical Journal*, 158(4):158, October 2019. ISSN 0004-6256, 1538-3881. doi: 10.3847/1538-3881/ab3a44. URL <https://iopscience.iop.org/article/10.3847/1538-3881/ab3a44>. 15
- [38] Thomas B. Kaiser. Laser ray tracing and power deposition on an unstructured three-dimensional grid. *Physical Review E*, 61(1):895–905, January 2000. doi: 10.1103/PhysRevE.61.895. URL <https://link.aps.org/doi/10.1103/PhysRevE.61.895>. Publisher: American Physical Society. 18, 19, 21
- [39] Thierry Dewandre, James R. Albritton, and E. A. Williams. Doppler shift of laser light reflected from expanding plasmas. *The Physics of Fluids*, 24(3):528–536, March 1981. ISSN 0031-9171. doi: 10.1063/1.863401. URL <https://pubs.aip.org/pfl/article/24/3/528/894917/Doppler-shift-of-laser-light-reflected-from>. 18
- [40] William H. Press, editor. *Numerical recipes: the art of scientific computing*. Cambridge University Press, Cambridge, 3. ed edition, 2007. ISBN 978-0-521-88068-8. 19
- [41] Jacob Williams. bspline-fortran, January 2024. URL <https://zenodo.org/records/8423936>. 19
- [42] Charles K. Birdsall and A. Bruce Langdon. *Plasma physics via computer simulation*. McGraw-Hill, New York, 1985. ISBN 978-0-07-005371-7. 20
- [43] T D Arber, K Bennett, C S Brady, A Lawrence-Douglas, M G Ramsay, N J Sircombe, P Gillies, R G Evans, H Schmitz, A R Bell, and C P Ridgers. Contemporary particle-in-cell approach to laser-plasma modelling. *Plasma Physics and Controlled Fusion*, 57(11):113001, November 2015. ISSN 0741-3335, 1361-6587. doi: 10.1088/0741-3335/57/11/113001. URL <https://iopscience.iop.org/article/10.1088/0741-3335/57/11/113001>. 20
- [44] Christophe Cornet and Dixon T.K. Kwok. A new algorithm for charge deposition for multiple-grid method for PIC simulations in r-z cylindrical coordinates. *Journal of Computational Physics*, 225(1):808–828, July 2007. ISSN 00219991. doi: 10.1016/j.jcp.2007.01.004. URL <https://linkinghub.elsevier.com/retrieve/pii/S0021999107000058>. 20
- [45] Brian M. Haines, D.E. Keller, J.A. Marozas, P.W. McKenty, K.S. Anderson, T.J.B. Collins, W.W. Dai, M.L. Hall, S. Jones, M.D. McKay Jr, R.M. Rauenzahn, and D.N. Woods. Coupling laser physics to radiation-hydrodynamics. *Computers & Fluids*, 201:104478,

- April 2020. ISSN 00457930. doi: 10.1016/j.compfluid.2020.104478. URL <https://linkinghub.elsevier.com/retrieve/pii/S0045793020300517>. 21, 24
- [46] J. Denavit and D. W. Phillion. Laser ionization and heating of gas targets for long-scale-length instability experiments. *Physics of Plasmas*, 1(6):1971–1984, June 1994. ISSN 1070-664X, 1089-7674. doi: 10.1063/1.870653. URL <https://pubs.aip.org/pop/article/1/6/1971/260717/Laser-ionization-and-heating-of-gas-targets-for>. 24
- [47] I. V. Igumenshchev, F. J. Marshall, J. A. Marozas, V. A. Smalyuk, R. Epstein, V. N. Goncharov, T. J. B. Collins, T. C. Sangster, and S. Skupsky. The effects of target mounts in direct-drive implosions on OMEGA. *Physics of Plasmas*, 16(8):082701, August 2009. ISSN 1070-664X, 1089-7674. doi: 10.1063/1.3195065. URL <https://pubs.aip.org/pop/article/16/8/082701/316526/The-effects-of-target-mounts-in-direct-drive>. 28
- [48] I. V. Igumenshchev, V. N. Goncharov, F. J. Marshall, J. P. Knauer, E. M. Campbell, C. J. Forrest, D. H. Froula, V. Yu. Glebov, R. L. McCrory, S. P. Regan, T. C. Sangster, S. Skupsky, and C. Stoeckl. Three-dimensional modeling of direct-drive cryogenic implosions on OMEGA. *Physics of Plasmas*, 23(5):052702, May 2016. ISSN 1070-664X, 1089-7674. doi: 10.1063/1.4948418. URL <https://pubs.aip.org/pop/article/23/5/052702/958965/Three-dimensional-modeling-of-direct-drive>.
- [49] M. Gatu Johnson, P. J. Adrian, K. S. Anderson, B. D. Appelbe, J. P. Chittenden, A. J. Crilly, D. Edgell, C. J. Forrest, J. A. Frenje, V. Yu. Glebov, B. M. Haines, I. Igumenshchev, D. Jacobs-Perkins, R. Janezic, N. V. Kabadi, J. P. Knauer, B. Lahmann, O. M. Mannion, F. J. Marshall, T. Michel, F. H. Séguin, R. Shah, C. Stoeckl, C. A. Walsh, and R. D. Petrasso. Impact of stalk on directly driven inertial confinement fusion implosions. *Physics of Plasmas*, 27(3):032704, March 2020. ISSN 1070-664X, 1089-7674. doi: 10.1063/1.5141607. URL <https://pubs.aip.org/pop/article/27/3/032704/1063027/Impact-of-stalk-on-directly-driven-inertial>. 28
- [50] I. V. Igumenshchev, W. Seka, D. H. Edgell, D. T. Michel, D. H. Froula, V. N. Goncharov, R. S. Craxton, L. Divol, R. Epstein, R. Follett, J. H. Kelly, T. Z. Kosc, A. V. Maximov, R. L. McCrory, D. D. Meyerhofer, P. Michel, J. F. Myatt, T. C. Sangster, A. Shvydky, S. Skupsky, and C. Stoeckl. Crossed-beam energy transfer in direct-drive implosions. *Physics of Plasmas*, 19(5):056314, May 2012. ISSN 1070-664X, 1089-7674. doi: 10.1063/1.4718594. URL <https://pubs.aip.org/pop/article/19/5/056314/596972/Crossed-beam-energy-transfer-in-direct-drive>. 29
- [51] William L. Kruer. *The physics of laser plasma interactions*. Frontiers in physics. CRC Press, Boulder, Colo. [u.a.] Westview, 2003. ISBN 978-0-8133-4083-8. 29
- [52] Jurij A. Kravcov and Jurij I. Orlov. *Caustics, catastrophes and wave fields*. Number 15 in Springer series on wave phenomena. Springer, Berlin Heidelberg New York, 2. ed edition, 1999. ISBN 978-3-540-64227-5. 29

- [53] Yury Alexandrovich Kratsov and Ning Yan Zhu. Theory of diffraction: heuristic approaches. Alpha Science International, Oxford, 2010. ISBN 978-1-84265-372-2. 29
- [54] N. A. Lopez and I. Y. Dodin. Metaplectic geometrical optics for ray-based modeling of caustics: Theory and algorithms. Physics of Plasmas, 29(5):052111, May 2022. ISSN 1070-664X, 1089-7674. doi: 10.1063/5.0082241. URL <https://pubs.aip.org/pop/article/29/5/052111/2847808/Metaplectic-geometrical-optics-for-ray-based>. 29
- [55] Shan-chieh Chang and Jian-Ming Jin. Computation of special functions. Wiley, New York, 1996. ISBN 978-0-471-11963-0. 30
- [56] A.A. Asatryan and Yu.A. Kravtsov. Fresnel zones of hyperbolic type from the physical point of view. Wave Motion, 10(1):45–57, January 1988. ISSN 01652125. doi: 10.1016/0165-2125(88)90005-4. URL <https://linkinghub.elsevier.com/retrieve/pii/0165212588900054>. 30
- [57] Yu.A. Kravtsov. IV Rays and Caustics as Physical Objects. In Progress in Optics, volume 26, pages 227–348. Elsevier, 1988. ISBN 978-0-444-87096-4. doi: 10.1016/S0079-6638(08)70177-X. URL <https://linkinghub.elsevier.com/retrieve/pii/S007966380870177X>. 30
- [58] R. K. Follett. LPSE data for ray-based CBET test cases, August 2022. URL <https://zenodo.org/record/6962934>. 30, 45
- [59] Jiachen Ding, Ping Yang, Michael I. Mishchenko, and Robert D. Nevels. Identify the limits of geometric optics ray tracing by numerically solving the vector Kirchhoff integral. Optics Express, 28(7):10670, March 2020. ISSN 1094-4087. doi: 10.1364/OE.389097. URL <https://opg.optica.org/abstract.cfm?URI=oe-28-7-10670>. 34
- [60] E. A. Williams, R. L. Berger, R. P. Drake, A. M. Rubenchik, B. S. Bauer, D. D. Meyerhofer, A. C. Gaeris, and T. W. Johnston. The frequency and damping of ion acoustic waves in hydrocarbon (CH) and two-ion-species plasmas. Physics of Plasmas, 2(1):129–138, January 1995. ISSN 1070-664X, 1089-7674. doi: 10.1063/1.871101. URL <https://pubs.aip.org/pop/article/2/1/129/261605/The-frequency-and-damping-of-ion-acoustic-waves-in>. 36
- [61] P. Michel, W. Rozmus, E. A. Williams, L. Divol, R. L. Berger, S. H. Glenzer, and D. A. Callahan. Saturation of multi-laser beams laser-plasma instabilities from stochastic ion heating. Physics of Plasmas, 20(5):056308, May 2013. ISSN 1070-664X, 1089-7674. doi: 10.1063/1.4802828. URL <https://pubs.aip.org/pop/article/20/5/056308/109013/Saturation-of-multi-laser-beams-laser-plasma>. 36
- [62] G. P. M. Poppe and C. M. J. Wijers. Algorithm 680: evaluation of the complex error function. ACM Transactions on Mathematical Software, 16(1):47, March 1990. ISSN 0098-3500, 1557-7295. doi: 10.1145/77626.77630. URL <https://dl.acm.org/doi/10.1145/77626.77630>. 37

- [63] Burton D. Fried and Samuel D. Conte. The Plasma Dispersion Function: The Hilbert Transform of the Gaussian. Academic Press, 1961. ISBN 978-1-4832-2929-4. 37
- [64] T. R. Boehly, V. A. Smalyuk, D. D. Meyerhofer, J. P. Knauer, D. K. Bradley, R. S. Craxton, M. J. Guardalben, S. Skupsky, and T. J. Kessler. Reduction of laser imprinting using polarization smoothing on a solid-state fusion laser. Journal of Applied Physics, 85(7):3444–3447, April 1999. ISSN 0021-8979, 1089-7550. doi: 10.1063/1.369702. URL <https://pubs.aip.org/jap/article/85/7/3444/491506/Reduction-of-laser-imprinting-using-polarization>. 37
- [65] D. H. Edgell, P. B. Radha, J. Katz, A. Shvydky, D. Turnbull, and D. H. Froula. Nonuniform Absorption and Scattered Light in Direct-Drive Implosions Driven by Polarization Smoothing. Physical Review Letters, 127(7):075001, August 2021. ISSN 0031-9007, 1079-7114. doi: 10.1103/PhysRevLett.127.075001. URL <https://link.aps.org/doi/10.1103/PhysRevLett.127.075001>. 37
- [66] A. Colaïtis, D. P. Turnbull, I. V. Igumenschev, D. Edgell, R. C. Shah, O. M. Mannion, C. Stoeckl, D. Jacob-Perkins, A. Shvydky, R. Janezic, A. Kalb, D. Cao, C. J. Forrest, J. Kwiatkowski, S. Regan, W. Theobald, V. N. Goncharov, and D. H. Froula. 3D Simulations Capture the Persistent Low-Mode Asymmetries Evident in Laser-Direct-Drive Implosions on OMEGA. Physical Review Letters, 129(9):095001, August 2022. ISSN 0031-9007, 1079-7114. doi: 10.1103/PhysRevLett.129.095001. URL <https://link.aps.org/doi/10.1103/PhysRevLett.129.095001>.
- [67] A Colaïtis, I V Igumenshchev, D P Turnbull, R Shah, D Edgell, O M Mannion, C Stoeckl, D W Jacob-Perkins, A Shvydky, R Janezic, A Kalb, D Cao, C J Forrest, J Kwiatkowski, S P Regan, W Theobald, V N Goncharov, and D Froula. 3D simulations of inertial confinement fusion implosions part 2: systematic flow anomalies and impact of low modes on performances in OMEGA experiments. Plasma Physics and Controlled Fusion, 65(1):014005, January 2023. ISSN 0741-3335, 1361-6587. doi: 10.1088/1361-6587/aca78d. URL <https://iopscience.iop.org/article/10.1088/1361-6587/aca78d>.
- [68] A Colaïtis, D Edgell, I Igumenshchev, D Turnbull, D J Strozzi, T Chapman, V Goncharov, and D H Froula. 3D simulations of inertial confinement fusion implosions part 1: inline modeling of polarized cross beam energy transfer and subsequent drive anomalies on OMEGA and NIF. Plasma Physics and Controlled Fusion, 65(1):014003, January 2023. ISSN 0741-3335, 1361-6587. doi: 10.1088/1361-6587/aca78e. URL <https://iopscience.iop.org/article/10.1088/1361-6587/aca78e>. 37
- [69] O. M. Mannion, I. V. Igumenshchev, K. S. Anderson, R. Betti, E. M. Campbell, D. Cao, C. J. Forrest, M. Gatu Johnson, V. Yu. Glebov, V. N. Goncharov, V. Gopalaswamy, S. T. Ivancic, D. W. Jacobs-Perkins, A. Kalb, J. P. Knauer, J. Kwiatkowski, A. Lees, F. J. Marshall, M. Michalko, Z. L. Mohamed, D. Patel, H. G. Rinderknecht, R. C. Shah, C. Stoeckl, W. Theobald, K. M. Woo, and S. P. Regan. Mitigation of mode-one asymmetry in laser-direct-drive inertial confinement fusion implosions. Physics

- of Plasmas, 28(4):042701, April 2021. ISSN 1070-664X, 1089-7674. doi: 10.1063/5.0041554. URL <https://pubs.aip.org/pop/article/28/4/042701/263531/Mitigation-of-mode-one-asymmetry-in-laser-direct>. 37
- [70] Dhrumir Patel, Riccardo Betti, Varchas Gopalaswamy, and Ka Ming Woo. Novel double-spike pulse shape for OMEGA cryogenic implosions. 2018:GO6.006, January 2018. URL <https://ui.adsabs.harvard.edu/abs/2018APS..DPPG06006P>. Conference Name: APS Division of Plasma Physics Meeting Abstracts ADS Bibcode: 2018APS..DPPG06006P. 51
- [71] D. Cao, R. C. Shah, S. P. Regan, R. Epstein, I. V. Igumenshchev, V. Gopalaswamy, A. R. Christopherson, W. Theobald, P. B. Radha, and V. N. Goncharov. Interpreting the electron temperature inferred from x-ray continuum emission for direct-drive inertial confinement fusion implosions on OMEGA. *Physics of Plasmas*, 26(8):082709, August 2019. ISSN 1070-664X, 1089-7674. doi: 10.1063/1.5112759. URL <https://pubs.aip.org/pop/article/26/8/082709/632047/Interpreting-the-electron-temperature-inferred>.
- [72] A. J. Crilly, B. D. Appelbe, O. M. Mannion, C. J. Forrest, V. Gopalaswamy, C. A. Walsh, and J. P. Chittenden. Neutron backscatter edge: A measure of the hydrodynamic properties of the dense DT fuel at stagnation in ICF experiments. *Physics of Plasmas*, 27(1):012701, January 2020. ISSN 1070-664X, 1089-7674. doi: 10.1063/1.5128830. URL <https://pubs.aip.org/pop/article/27/1/012701/262967/Neutron-backscatter-edge-A-measure-of-the>. 51
- [73] James McHardy. An introduction to the theory and use of SESAME equations of state. Technical Report LA-14503, 1487368, December 2018. URL <https://www.osti.gov/servlets/purl/1487368/>. 51
- [74] A.J. Crilly, N.P.L. Niasse, A.R. Fraser, D.A. Chapman, K.W. McLean, S.J. Rose, and J.P. Chittenden. SpK: A fast atomic and microphysics code for the high-energy-density regime. *High Energy Density Physics*, 48:101053, September 2023. ISSN 15741818. doi: 10.1016/j.hedp.2023.101053. URL <https://linkinghub.elsevier.com/retrieve/pii/S1574181823000198>. 51



## **Permissions**